npj | natural hazards

Article

https://doi.org/10.1038/s44304-026-00186-8

Climate extremes and urbanization drive flood tipping points at the city–river interface

Check for updates

Dingyu Xuan[1,2] ✉, M. Ani Hsieh[3,4], Leandro S. Pongeluppe[5], Mackenzie M. Weaver[1], Michael E. Mann[1], Douglas J. Jerolmack[1,4] & Hugo N. Ulloa[1] ✉

Hurricane Ida struck the U.S. East Coast in August 2021, driving the Schuylkill River in Philadelphia to a record discharge nearly 100 times its average flow. Ida exposes the growing challenge of predicting urban flooding arising from coupled rainfall–runoff and river–tide–landscape interactions that coarse models cannot resolve. Here, we address this gap with a street-resolving flood model that integrates LiDAR-derived terrain, bathymetric surveys, and land-use-based surface friction across Philadelphia's watershed to reproduce Ida's flood. We show that soil saturation, impervious surfaces, and fragmented infrastructure amplify pluvial flooding, increasing exposure in both low- and high-income communities. Scenario simulations reveal a flood tipping point: for river return periods exceeding 100 years, the inundated area grows logarithmically, with an additional 2–7% increase in flooding when peak discharge coincides with high tide and up to ~15% under projected sea-level rise by 2100. As extreme rainfall intensifies and return periods shorten, this tipping point will be crossed more often, demanding integrated forecasting and adaptive planning in vulnerable, low-lying, rapidly urbanizing regions.

Hurricane Ida made landfall in Louisiana as a Category 4 hurricane on August 29, 2021, producing strong winds, storm surges, and intense rainfall that devastated the Gulf Coast[1]. As it moved inland (SI Fig. S1), the storm's remnants and seven tornadoes that struck Philadelphia between September 1–2 triggered unprecedented discharge and a 1-in-100-year flood along the Schuylkill River, causing widespread damage[2] (SI Table S2). Extreme hydrometeorological events (EHMEs) like Ida already cause average global losses of $136.7 billion annually (2003–2022)[3], surging to over $320 billion in 2024 alone[4]. Rain-driven floods are projected to intensify as climate extremes intensify and urbanization expands, thereby constraining rivers and altering floodplain dynamics[5,6]. In tidally influenced rivers, sea-level rise (SLR) and stronger tropical cyclones further amplify flood severity and human vulnerability[7,8]. Currently, 13.3% of the U.S. population—over 40 million people—is exposed to a 1-in-100-year flood[9], yet future flood risks in urban and coastal corridors remain poorly quantified[10,11], relying on coarse models that obscure critical compound drivers and limit effective mitigation in densely populated metropolitan regions[12]. Philadelphia exemplifies this challenge: as the second-most populous city on the U.S. East Coast (1.5M), bounded by the Delaware River to the east and bisected by the Lower Schuylkill River (Fig. 1a–c).

The Schuylkill River rushes through bedrock rapids as it enters Philadelphia, transitioning from the Piedmont to the Coastal Plain, where urban development is concentrated[13]. Historically, the Schuylkill served as both a sewer and a navigable waterway during the 19th century, supporting Philadelphia's rapid industrial and population growth from around 41,000 residents in 1800 to nearly 1.3 million by 1900[13]. By the 20th century, flood-control measures—channelization and levee construction—were introduced to reduce mounting flood risks[14], such as the Fairmount Dam. These interventions enabled dense riverside development but also severed the river's connection to its natural floodplain, diminishing its ability to absorb and regulate extreme events. Meanwhile, average annual discharge of the river (25–160 m^3/s) has increased since 1931 with a modest yet statistically significant rising trend (0.3 $m^3/s/a$) (SI Fig. S2a), typically peaking in spring but now showing more frequent and extreme autumn peaks from hurricane intensification under climate change[15,16] (SI Fig. S2b). Current infrastructure struggles with intensifying EHMEs, as demonstrated by Hurricane Ida. A broader knowledge gap persists in understanding how urban rivers, particularly those tidally influenced, respond to compounding stressors such as EHMEs and SLR. This challenge extends far beyond Philadelphia, affecting cities worldwide where fluvial–tidal interactions remain poorly understood

[1]Department of Earth and Environmental Science, University of Pennsylvania, Philadelphia, PA, USA. [2]Department of Civil and Environmental Engineering, Imperial College London, London, UK. [3]General Robotics, Automation, Sensing, and Perception (GRASP) Lab, University of Pennsylvania, Philadelphia, PA, USA. [4]Department of Mechanical Engineering and Applied Mechanics, University of Pennsylvania, Philadelphia, PA, USA. [5]The Wharton School, University of Pennsylvania, Philadelphia, PA, USA. ✉e-mail: dingyu.xuan24@imperial.ac.uk; ulloa@sas.upenn.edu

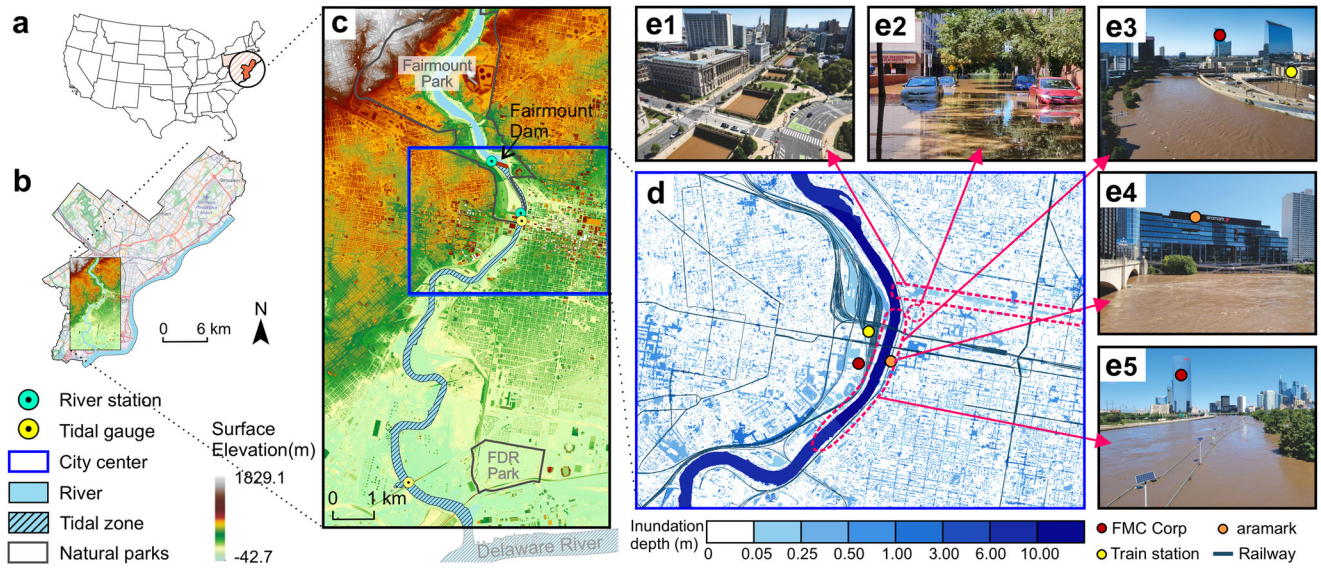


Fig. 1 | Map of research area and flood inundation of the Center City validated by drone images. **a** The location of Philadelphia in the US. **b** Research area in Philadelphia overlaid with Open Street Map. **c** Surface elevation of the study area. **d** Flood inundation map based on the Digital Surface Model (DSM) with railway lines overlaid. **e** Drone images with identifiable landmarks were collected from social media, illustrating the actual inundated areas: **e1** Vine Street Expressway; **e2** the area in Center City Philadelphia; **e3** Amtrak rail yards; **e4** in front of the Aramark Global Headquarters; **e5** the Schuylkill Boardwalk, which is nearly submerged; (**e1**–**e5** credit: Mark Henninger).

but can amplify flood impacts[17–19]. While hydrodynamic models hold promise for urban flood forecasting and resilience planning, several challenges remain: limited availability of detailed terrain data, sparse observations for model calibration, difficulties in integrating heterogeneous datasets, and trade-offs between computational efficiency and storage for fine-scale simulations[20–22].

Here, we develop a high-resolution flood modeling framework for the Philadelphia-Schuylkill system, employing the Graphics Processing Unit (GPU)-accelerated LISFLOOD-FP numerical framework[23], to resolve street-level inundation dynamics. Our findings reveal a dual amplification of flood risk driven by urbanization: impervious surfaces increase runoff by reducing infiltration, while engineered infrastructure forms drainage bottlenecks that impede flow toward major waterways. We also identify Hurricane Ida's disproportionate impact on both low- and high-income populations, who experienced comparable flood exposure—underscoring the need for targeted protection of vulnerable communities. We find that the Schuylkill River's current 100-year flood capacity ($Q_{100} \approx 3,480 m^3/s$) represents a tipping point: surpassing it triggers nonlinear increases in inundation extent. Additionally, climate change and urbanization have compressed return periods, as revealed by our frequency analysis. Flows once considered 1-in-50-year events (e.g., $2,000 m^3/s$ in the 1950s) now occur statistically every 3 years. Rainfall and topography primarily govern flood patterns, whereas tidally modulated downstream water levels can further expand inundation in riparian areas. While these findings provide critical guidance for city managers, planners, and policymakers in Philadelphia, the challenges we uncover and tackle are in fact representative of riverine and coastal cities globally, each influenced by their own distinct urban landscape, environmental, and socio-economic contexts.

Results

Modeling framework

Our model integrates the city's first 5-m LiDAR-derived terrain model and the latest Schuylkill River bathymetry survey (SI Fig. S3) to best calculate flow direction. Surface roughness is calibrated using the National Land Cover Database based on the relationship between frictional Manning coefficients and land use ("Methods"). The model solves for the interaction among upstream river flow, downstream tidal elevation, and rainfall across the domain, using these three primary boundary conditions. The outputs include water depth, flow velocity, and discharge.

To validate the model's ability to reproduce flooded areas within the floodplain, we used citizen-reported data, drone and satellite imagery, and on-site observations. High-resolution drone images from Hurricane Ida show striking agreement with simulated inundation, particularly along the east bank of the Schuylkill River near Center City, where the model captures severe flooding across Fairmount Park, the museum and financial districts, and major transport corridors (Fig. 1d, e). Using satellite-based flood extent and in situ hydrodynamic measurements, we further estimate that the model reproduces 68% of inundated urban areas and more than 90% of river discharge and water levels along the channel, providing robust support for its application to compound flood risk in dense river–city systems.

Uncovering the Ida flood footprint in Philadelphia

Like many cities built along tidally influenced rivers, Philadelphia's flood severity is shaped by three key factors: watershed rainfall, river discharge, and tidal surges. The Fairmount Dam marks the upstream tidal limit of the Schuylkill River (Fig. 1c). Downstream, the tidally affected reach flows between Center City to the east and major hospitals and universities to the west, flanked by dense transportation infrastructure (Fig. 1d). Our analysis reveals that the east bank is particularly vulnerable to flooding due to its lower elevation, direct connectivity to roadways and tunnels, and localized erosion. This risk is most pronounced in the central region of the Lower Schuylkill (Fig. 1d).

Flooding also significantly impacted transportation infrastructure. Nearly all railway lines adjacent to the river experienced disruption: east bank lines, situated closer to the channel, were primarily affected by overbank flow, while west bank lines were more susceptible to intense rainfall (Figs. 1e3–5). The convergence of fluvial and pluvial drivers created a substantial hazard, particularly along the east bank, with floodwaters extending into the urban core.

But why was Hurricane Ida's impact in Philadelphia so severe? Extensive impervious surfaces and pre-saturated soils likely intensified surface runoff, increasing river discharge. These conditions highlight the role of urbanization and antecedent hydrometeorological states in amplifying flood severity during extreme events.

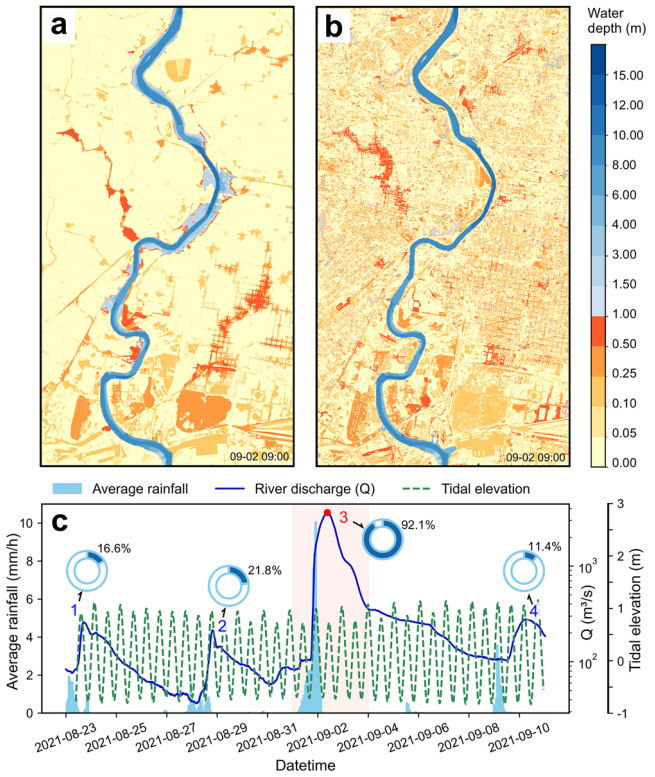


Fig. 2 | Inundation map resulting from Hurricane Ida using different elevation models. Flood inundation based on DTM (**a**) and DSM (**b**) at 9 a.m. on September 2, 2021, shown as the red point in **c**. **c** Time series of average rainfall for the whole upstream watershed, river discharge at the upstream boundary condition, and tidal elevation at the downstream boundary condition. The numbers along the discharge line correspond to four distinct peaks in river discharge, with the adjacent doughnut charts illustrating the respective runoff coefficients. Each complete doughnut chart represents the cumulative rainfall leading up to each peak, while the blue-shaded portion depicts the proportion of that rainfall converted into surface runoff. The light-orange-shaded area indicates the occurrence of the extreme rainfall event, which took place between September 1 and September 3, 2021.

Urbanization and prior hydrometeorology shaping flood risk

To examine the role of urbanization in the flood severity, we conducted numerical simulations of the Lower Schuylkill River during Hurricane Ida (September 1–3, 2021) using two digital elevation models: a bare-earth Digital Terrain Model (DTM) and an infrastructure-inclusive Digital Surface Model (DSM) (Fig. 2a, b; SI Text 2). The DTM-based simulation reveals more extensive riverine flooding, with surface runoff naturally concentrating along topographic lows and channel networks. In contrast, the DSM simulation—incorporating buildings, roads, and levees—exhibits less overbank flooding but broader distributed inundation across the urban landscape.

This spatial pattern reflects two key effects of urbanization. First, engineered riverbanks and levees constrain lower-Return-Period floods, reducing overtopping and limiting floodplain spread. Second, impervious surfaces and built structures impede drainage, trapping water in depressions and generating localized, stagnant flooding. These shallow inundations disproportionately affect pedestrian and vehicular mobility in low-lying urban neighborhoods. Overall, the DSM scenario (Fig. 2) results in a 30% increase in inundated area and an ~8% increase in downstream peak flow (SI Fig. S5) relative to the DTM (Fig. 2), underscoring the combined influence of urban form and topography on flood hazards in cities such as Philadelphia.

In addition to reduced infiltration caused by urbanization, antecedent soil moisture critically influences flood severity during EHMEs. Prior to Hurricane Ida, two moderate storms (events 1 and 2 in Fig. 2c) progressively saturated the watershed. We assessed infiltration-runoff dynamics using the runoff coefficient ($\mathcal{C}$), defined as the fraction of precipitation converted to surface runoff (SI Text 5). Four discharge peaks were analyzed: "peak 1" and "peak 2" before Ida, "peak 3" during the main flood, and "peak 4" after recession. Although rainfall before "peak 2" was lighter than before "peak 1", it generated more runoff, indicating that the 4-day dry interval was insufficient for the soil to recover its infiltration capacity. This suggests that soils were already near saturation 3 days before Ida. Consequently, nearly all rainfall during the main event was converted to runoff. While cumulative rainfall before "peak 3" was only 5.5 times that of "peak 2", river discharge was 23.2 times greater, corresponding to a peak $\mathcal{C}$ of 92.1%. One week later, $\mathcal{C}$ it dropped below 12.0%, signaling a return to baseline hydrologic conditions. These findings highlight the critical role of antecedent hydrologic conditions in shaping EHME-induced flooding. Ignoring pre-event soil moisture can lead to substantial underestimation of runoff and flood severity in urban flood models.

The strong influence of both urban form and hydrologic state on inundation patterns raises a pressing question for impact assessment and climate adaptation: Who is most at risk during extreme weather events? This concern is especially acute in densely populated cities with socio-economic disparities and aging infrastructure, where compound flooding can exacerbate vulnerabilities and amplify inequities.

Flood inequality and economic impacts in Philadelphia

We quantified individual-level flood risk using a Socioeconomic Vulnerability Index (SEVI) that averages eight indicators—housing burden, language, educational attainment, age, race, employment status, and poverty—following[24] (Fig. 3a; "Methods"). The SEVI serves as a proxy for socioeconomic status and stratifies residents into five groups. Across groups, housing burden, low educational attainment, and racial discrimination contribute most, whereas age contributes least to this study site.

Our analysis reveals that both the lowest and highest SEVI groups are disproportionately vulnerable to flooding. Despite accounting for relatively small shares of the total inundated area, these groups exhibit the highest rates of population exposure—over 20% in both cases (Fig. 3b). For high-SEVI communities, heightened exposure likely stems from insufficient flood preparedness and systemic neglect of environmental protections[25]. In contrast, low-SEVI populations face increased flood risk due to extensive impervious surfaces and localized land subsidence (measured at 1–3 mm per year) driven by groundwater withdrawal and compaction from dense infrastructure[26,27]. While proximity to water bodies offers low-SEVI residents recreational and aesthetic benefits, it also amplifies their exposure to fluvial hazards. Moreover, flooding in these economic hubs, such as Center City, can lead to substantial indirect losses, including business disruptions, and infrastructure damage that delay post-disaster recovery.

In terms of total flood-affected area, the 40–60% SEVI group experienced the most widespread inundation, reflecting that most census tracts within this study site fall in this socioeconomic vulnerability range in Philadelphia relative to Pennsylvania. Beyond these densely populated regions, urban green spaces such as Fairmount Park and FDR Park serve a dual function: providing essential recreational and cultural access while acting as natural hydrological buffers. These parks mitigate downstream flood impacts by absorbing and temporarily storing stormwater. However, during sequences of moderate rainfall followed by extreme events, their storage capacity may be exceeded, leading to increased surface runoff and more severe floods.

To better assess the economic and financial damages caused by Hurricane Ida in Philadelphia relative to other regions of Pennsylvania, we estimated the zipcode-level impact using U.S. Small Business Administration (SBA) disaster loan data[28,29] (SI Text 4). This analysis reveals a pronounced disparity in Ida's economic effects across Pennsylvania: on average, verified losses were significantly higher in Philadelphia, USD 160,061 per zipcode, while approved SBA disaster loans increased by only USD 13,997—a statistically non-significant difference (Fig. 3d). These results indicate that, although Philadelphia sustained disproportionately greater damage,

monetary support did not scale with the magnitude of its losses. The divergence between verified losses and loan disbursements indicates structural limitations in post-disaster financial mechanisms, particularly in dense urban areas where exposure and damage intensity are highest (SI Tables S3 and S4).

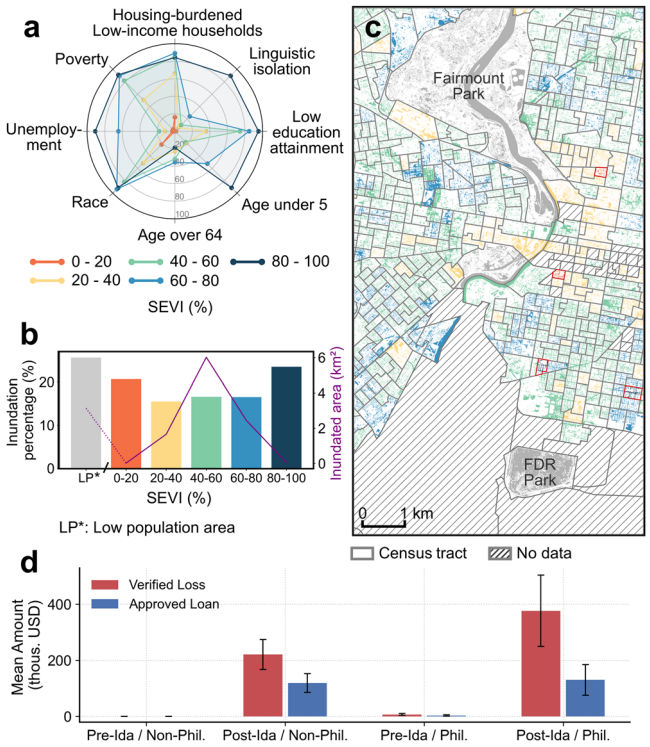


Fig. 3 | Effect of socioeconomic situation on flood inundation and economic consequences of this event. a Eight components of different socioeconomic vulnerability indices (SEVI) and their contributions in different SEVI groups. The values for each component represent the average values within each SEVI group (see "Methods"). Here, a higher SEVI indicates a more impoverished socioeconomic situation. **b** Inundation percentages and areas of different SEVI groups for this 2021 flood event. SEVI groups exclude the census tract with a population density less than 10 people per square kilometer, shown as the gray region in **c**. **c** Inundation in regions with different SEVI. Different colors indicate different SEVI groups shown in **b**. The most affected groups (0–20% and 80–100%) are highlighted with red boundaries. **d** Verified losses and approved loans in Pennsylvania Pre- and Post-Ida Hurricane. Data from the Small Business Administration US at the zipcode-year level.

These estimated impacts were further used to assess the disaster's financial implications. Across a range of discount and default rate sensitivity scenarios (SI Fig. S4, and Table S5), the resulting net present values remain consistently negative, ranging from USD 19.9 to USD 21.4 million. From a societal perspective, Hurricane Ida imposed a significant and persistent welfare loss on Philadelphia, only partially offset by existing governmental credit-based relief. Together, these findings underscore the disproportionate economic exposure of urban centers, such as Philadelphia, to climate extreme disasters and their limited financial resilience even under dedicated federal assistance programs.

Schuylkill in a changing climate

We analyzed return periods for the Schuylkill River over the past century and identified the 2021 flood as the largest fluvial event on record. The relationship between discharge and return periods follows a logarithmic trend, which we used to extrapolate peak flows for more extreme events (Fig. 4a). A more detailed examination of annual peak flows reveals a sustained upward trend, particularly for high-return-period events. Frequency analyzes of successive 20-year periods confirm this intensification (Fig. 4b, c). Although both annual peak and mean streamflow have increased significantly since 1931 (SI Fig. S6), peak flows have risen about 30 times faster than the mean. This disproportionate increase points to intensified short-duration, high-intensity rainfall events and shorter return periods for extremes. Importantly, a four-decade analysis (1970–2010) found that impervious surface across Philadelphia remained stable despite active internal land-use transitions[30]. Coupled with projections of near-consistent land types throughout the 21st century[31], these patterns offer direct evidence of climate-driven extremes in the local hydrologic regime.

To assess the implications of these trends, we simulated flood inundation across eight synthetic hydrographs, representing return periods from 5 to 5000 years. These were generated using the extrapolated discharge relationship $Q = a_0 \ln(r) + b_0$ and a standardized hydrograph based on historical events (SI Text 5, Fig. S7). Six cross-sections—three upstream and three downstream of Fairmount Dam—were selected to evaluate spatial variations of the City-River interface in response to the flood (Fig. 5a). River levels rise predictably with increasing discharge, but a sharp inflection occurs near the 100-year threshold. Below this threshold, floodwaters are typically contained within engineered riverbanks; above it, inundation expands rapidly in a logarithmic fashion (Fig. 5b), revealing the nonlinear escalation of flood hazard.

This nonlinear behavior is tightly linked to local topography and human infrastructure. During events with return periods shorter than 100 years, floodwaters remain largely confined by steep channelized banks and auxiliary structures such as raised terraces and refuge islands. However, floods with longer return periods exceed the capacity of both primary and

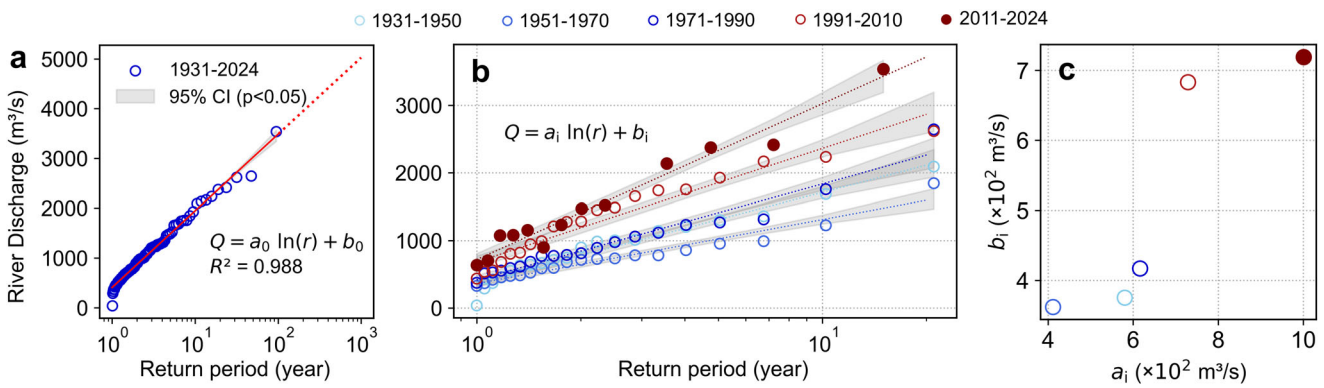


Fig. 4 | River discharge and flood inundation across different return periods. River discharge frequencies for the Schuylkill River are analyzed over the past century (**a**) and by every 20-year interval (**b**), with return periods estimated using the annual maxima series and the Weibull plotting position formula. Logarithmic trend line follows $Q = a_i \ln(r) + b_i$, with coefficients' values shown in **c**; for the full period, $a_0 = 667\ m^3/s$, $b_0 = 416\ m^3/s$. All fits yield $R_i^2 > 0.93$. Gray shaded areas indicate 95% confidence intervals.

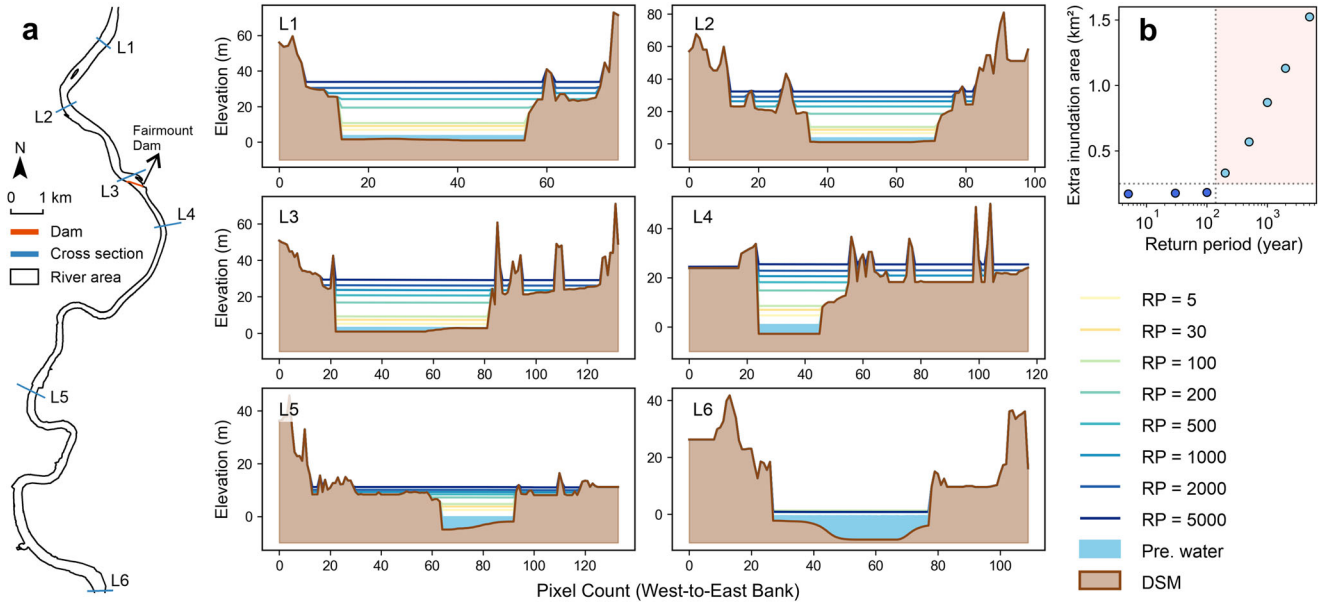


Fig. 5 | Cross sections and inundation extents of the Schuylkill River under different return periods (RP). a Top-down view of the Schuylkill River showing six selected cross sections near existing gauge stations. Three of these sections are situated upstream of the dam, while the remaining three are downstream. The "Pre. water" area represents the initial water level accumulated during the model's spin-up process. **b** River flood inundation areas for each RP, excluding the surface area of the Schuylkill River under pre-flood conditions. The light orange shaded area illustrates the logarithmic range of inundation growth, indicating that a critical flood threshold lies above the 100-year RP inflow.

secondary defenses, inundating wider urban areas (Fig. 5, panels L1–L6). Given the documented rise in extreme discharges (Fig. 4b, c), what is currently classified as a 100-year flood may become significantly more frequent. This evolving threat is compounded by tidal dynamics and SLR, which amplify overbank flooding and extend inundation into areas previously considered low risk.

Tides and sea level rise (SLR)

The interaction between the flood wave triggered by Hurricane Ida and a low but rising tide (Fig. 2c, "peak 3") raises the question of how downstream surface water elevation $\eta(t)$—modulated by tides at short timescales and SLR over long timescales—influences flood extents along the Lower Schuylkill River.

To quantify tidal influences, we performed spectral analysis of $\eta(t)$ over a 2-year period, identifying dominant tidal constituents and their key properties: amplitude, phase, and period (SI Text 6, Fig. S8). Semi-diurnal tides emerged as the primary drivers of variability, producing daily fluctuations that shift with the 14.7-day spring–neap cycle (SI Fig. S9). We also detected the annual King tide, which sets extreme tidal conditions downstream of Fairmount Dam. Because tidal stage and river discharge are statistically independent (SI Fig. S11), we applied harmonic analysis to reconstruct tidal behavior and assess compound flood risk scenarios (SI Text 8). We simulated worst-case flooding by combining the King tide with projected SLR trajectories.

Under projected SLR scenarios for 2100[32], the expansion of inundation in a 100-year flood is limited, suggesting that flows are less likely to exceed the tipping point when only coastal drivers are considered. In contrast, for a 1000-year flood event, an additional 100,000 m^2 could be inundated along the Schuylkill River (Fig. 6a), potentially affecting 5–12 city blocks or over 200 properties. To quantify the effect of extreme tide conditions on fluvial flooding, we computed the difference of inundated areas driven by the highest and lowest tide amplitude over a year. This difference increases sharply for return periods between 100 and 1000 years (Fig. 6b), primarily because the flood wave is less restricted after overtopping engineered levees and spreads through floodplains before reaching secondary barriers (Fig. 6c). On the west bank, natural terraces provide this secondary barrier, while on the east bank, a combination of built structures and elevated landforms—especially in the river's upper reach—play this role. Once floodwaters reach the second barriers, the floodplain becomes fully submerged, and additional tidal influence has a limited effect, as indicated by the leveling off inundated area beyond the 1000-year return period.

Overbank flow analysis along the tidally influenced reach (Fig. 6d) reveals consistently higher flood vulnerability on the east bank, corroborating both drone observations and model results from Hurricane Ida. The west bank, on the other hand, especially between 2 and 4.2 km, remains comparatively protected. A critical high-risk zone emerges near 2.2 km on the east bank, between the Vine Street Corridor (Fig. 1e2) and Market Street Bridge, where SLR amplifies flood risk to underground transportation infrastructure. These findings underscore the spatial variability of tide-modulated flood hazards and highlight the importance of targeted, site-specific adaptation strategies along the Lower Schuylkill River.

Changing storm characteristics

Past studies[33] have demonstrated that projected changes in tropical cyclone storm surges add to sea level rise in increasing coastal risk along the U.S. mid-Atlantic coast. Using a tropical cyclone down-scaling method driven by large-scale climate model simulations, Garner et al.[33] found that increases in both hurricane intensity and hurricane size (as measured by radius of maximum wind) contribute to increased likelihood of very large storm surges with continued warming. They focused specifically on New York City's Battery Park and the likelihood of future Superstorm Sandy-like inundation events, the return period of which is estimated to decrease from ~25 years today to ~5 years mid-century in a fossil fuel-intensive policy scenario. A similar analysis could be applied to the Schuylkill River catchment to assess the combined role of sea level change and changing storm characteristics in future projected coastal flooding risk for the Schuylkill watershed.

Discussion

Hurricane Ida produced record flooding on the Schuylkill—a nominal 1-in-100-year event. Century-scale records show such extremes are becoming more frequent and intense, with peak flows shifting from spring snowmelt to late-summer, often tropical, storms. These trends demand climate-informed risk assessment.

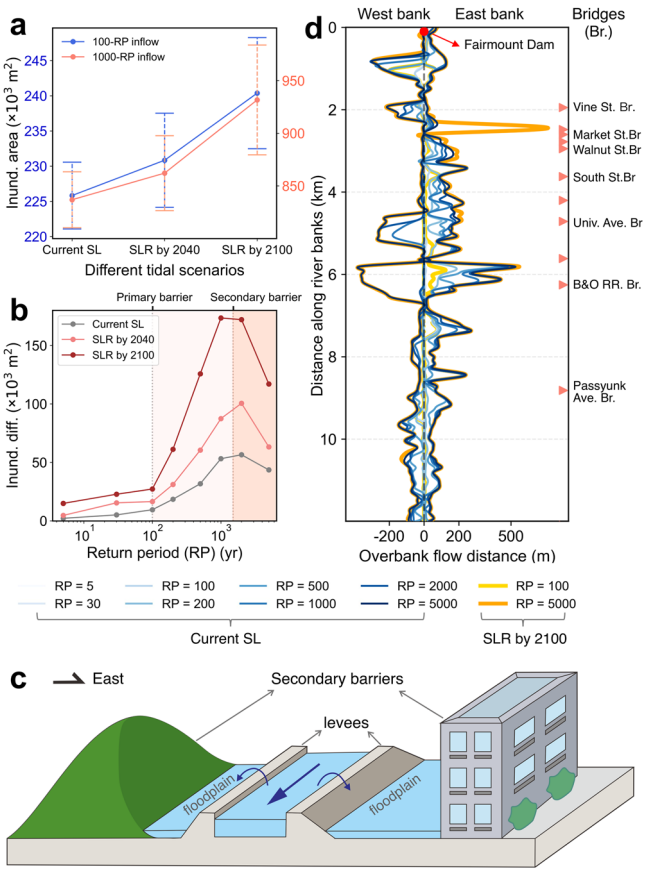


Fig. 6 | The impact of tidal phases and levels on inundation patterns and their combined effect with river discharge under different return periods (RP). a The scatter plot shows the average inundated area under 100-year and 1000-year RP river inflows, with dashed lines representing the range of inundation caused by extreme tides conditions, i.e., between the lowest and the King tide. In most cases, the largest inundated areas correspond to King tide conditions, and the lowest areas align with the lowest tide. Projected sea level rise (SLR) is based on localized estimates along the Delaware River, with increases of 0.5 meters by 2040 and 1.4 m by 2100[32]. **b** Differences in inundated area between King tide and the lowest tide in 2021 are shown across various river inflow RPs. The King tide and the lowest tide were aligned with the river discharge peak in the corresponding hydrograph for each simulation. **c** Schematic diagram of the primary and secondary barriers. **d** Overbank flow distance for various RPs river flows within the tidally affected section of the river. Distance along the river (*y*-axis) is measured relative to the Farimount Dam. Bridge names on the right are used for positioning (see SI Table S6 for full names).

Urbanization and wet antecedent soils amplify floods: impervious cover curtails infiltration and fragments flow paths, producing localized pooling rather than the channelized flooding typical of rural basins[34]. However, the detailed mechanisms of which parameters affect infiltration and recovery dynamics need further investigation. As heavy rain-bands move inland[35], cities like Philadelphia face more fluvial flooding—even without local rain. In our simulations, levees and embankments contain moderate events while buildings act as secondary barriers; once flows exceed the 100-year level, inundation expands rapidly. Designed for stationary hydrology, these defenses under-perform in a changing climate[36]. A ~30 mm storm (~2 mm/h) can take ~1 week to drain, so closely spaced storms saturate soils, boost runoff, and stress storm-water systems. Despite omitting subsurface drainage, the model reproduces Ida-driven flooding and identifies priority upgrade areas.

Our modeling framework integrates land use, urban infrastructure, rainfall, river discharge, and tides, but several uncertainties constrain our inferences. Near-term upgrades include spatially variable infiltration, explicit subsurface drainage, and wind effects on river dynamics and surge. Evaporation was neglected, given its small contribution (~0.3% of basal discharge). Morphology is static, though extreme flows can reshape channels[37,38]. On the Schuylkill, suspended sediment concentration rises sharply once riverbed shear exceeds ~24 Pa (discharge > 100m^3/s, SI Fig. S10); sediment records cover less than 10 years (1959–1968), underscoring monitoring gaps (SI Text 7).

Given these bounds, compound controls remain decisive in the tidally influenced Lower Schuylkill: risk spikes when river peaks coincide with high tide, and SLR amplifies this hazard. With ~1.4 m SLR by 2100, a 100-year flood could expand inundation by up to 15%, with larger increases for rarer events. Flood extent and pathways reflect hydrology and the built environment; mapping these constraints reveals hotspots and areas where riverine risk shifts to rainfall-driven flooding. Neighborhoods > 500 m from the river generally face lower fluvial exposure, though local topography and drainage still govern residual risk (SI Fig. S12).

Effective risk reduction requires geographically tailored strategies. The east bank's proximity to major roads and transit concentrates riverine exposure; the higher west bank's flat lands and rail yards are more prone to pluvial flooding. Both high- and low-income groups are exposed, but in different ways: higher-income riverfront and Central Business District can face elevated exposure from subsidence and infrastructure loading, while lower-income communities may lack preparedness resources and experience prolonged recovery, including public-health risks from sewage contamination[39]. Quantitative assessments of long-term socio-economic impacts (displacement, unemployment, educational disruption, mental health) remain scarce[25].

Despite data constraints—especially acute in under-resourced regions[21]—hydrodynamic models remain essential for resilience planning under evolving hydrometeorology[40,41]. Rising peak discharges for a given return period and pervasive SLR argue for climate-adaptive, not fixed-in-time, infrastructure to attenuate flood waves[42–44]. Nature-based solutions (e.g., Fairmount Park and FDR Park as stormwater "sponges") can cost-effectively complement gray systems[45,46]. Expanding access to high-resolution topography, precipitation forecasts, and high-performance modeling enables robust, real-time flood forecasting to protect vulnerable populations and critical assets. Philadelphia's priorities are: (i) compound-aware standards for capital projects (joint rainfall–river–tide–SLR design events; updated maps/codes); (ii) green–gray hybrids—floodable open spaces and expanded storage in Fairmount and FDR Parks—paired with hardened utilities and rail yards[45,46]; (iii) real-time forecasting using high-resolution topography and ensemble precipitation; and (iv) equitable adaptation that directs investment where hazard intersects socioeconomic vulnerability, and prioritizes critical services in frontline neighborhoods. Closing sediment, morphology, and drainage data gaps will reduce model uncertainty and sharpen prioritization[42–44].

We present a general approach to map flood risk from climate extremes in urban riverine systems. Using the Philadelphia–Schuylkill system as an example, we show that compound interactions among river discharge, tides/SLR, and the built environment recur across coastal cities, offering a transferable framework for site-specific, equitable adaptation.

Methods

LISFLOOD-FP model description

LISFLOOD-FP numerical solver is a 1D-2D raster-based hydrodynamic model based on the shallow water equations[23] (SI Text 1), which enable the modeling of spatially and temporally varying processes like precipitation and local water discharges; it can be directly downloaded from Zenodo (https://zenodo.org/records/6912932). Here, we used the state-of-the-art acceleration hydrodynamic solver LISFLOOD-ACC[23] as a local inertial scheme to numerically resolve the water flow throughout a uniform grid describing the urban landscape, the floodplain, and the river channel[47,48]. This solver has been shown to have high fitting accuracy with real inundations and runs with NVIDIA GPU cores to significantly enhance the computational efficiency[23].

Watershed landscape and friction

The hydraulic resistance encountered by the river flow due to the land surface characteristics and the riverbed's composition is quantified by Manning's frictional coefficient (n). This coefficient exhibits spatial variability and undergoes minor temporal changes. To establish the spatial distribution of the Manning coefficient within our study area, we have leveraged the United States Geological Survey (USGS) National Land Cover Dataset to analyze the current land use following[49]. The determined Manning coefficient ranges from 0.027 to 0.160. This detailed mapping of the landscape friction allows capturing the subtle variability in hydraulic resistance across the urban watershed of the Lower Schuylkill River (SI Fig. S14).

River discharge analysis

We conducted a frequency analysis to determine return periods for the Schuylkill River using historical peak discharge data from 1931 to 2024. Data prior to 1990 were based on the peak of daily average discharge, owing to the lower temporal resolution at that time, resulting in slight smoothing of peak values. Data from 1991 onward utilized peak flow values derived from 30-min interval measurements. When comparing peak flows across consecutive 20-year periods, the return period was recalculated because it is correlated with the length of the dataset (SI Text 5).

We used a long-time series of river discharges to analyze the single-peaked hydrograph of the Schuylkill River and further design flood hydrographs of more severe river scenarios. The time when the river flow peaks is defined as the origin, with time values before and after, negative and positive, respectively. The river discharge was scaled to 0 to 1 based on its proportion in the peak flow. The shape of a single-peaked hydrograph of the Schuylkill River is generally similar, so we assumed self-similarity in extrapolating flood waves to higher return periods. Rainfall intensities and associated river flows tend to follow the Gamma distribution[50]. However, this distribution does not capture the recession limb of river flows, so exponential functions are used to model the withdrawal of flows[51]. Two equations based on the gamma distribution and exponential function, respectively, were used to fit the shape of the hydrograph (SI Text 5). The hydrograph for a higher return period is designed by multiplying the fitted function by the calculated peak flow for a given return period based on the "similar-shape" assumption.

Tidal analysis

We used the Lomb-Scargle Periodogram Analysis, a spectral-density analysis method that is suitable for unequally spaced datasets[52], to detect the frequency of periodic signals of the Schuylkill River within the latest 2 years of tidal elevation data. Our results showed that the Schuylkill River is dominantly tidally modulated by the Lunar (M_2) and the Solar (S_2) semi-diurnal tides, and K_1 and O_1 diurnal tide. Thus, we used four Fourier modes to fit and model the tidal elevation signal as a function of time:

$$\eta(t) = \eta_0 + \sum_{i=1}^{4} A_i \sin\left[2\pi \frac{(t+t_0)}{T_i} + \phi_i\right], \quad (1)$$

$$t_0 = \mathrm{T}_0\,(\mathrm{TP}_i - \mathrm{TP}_0). \quad (2)$$

where $\eta_0 = 0.074$m. A_i, T_i, and ϕ_i are the amplitude, period, and phase of each tidal constituent, with values shown in SI Table S7. t_0 is 0 in the real flood case, yet it varies based on different TPs. TP_i represents a different tidal phase (SI Fig. S13), while TP_0, equal to 0.42, is the phase during the real event. T_0 in Eq. 2 is a constant representing the semidiurnal period, approximately equal to 0.5 days.

To assess the relationship between river peak discharge and tidal levels, we computed Spearman and Kendall rank correlation coefficients. Both values indicate statical significance (Spearman = −0.124, $p = 0.009$; Kendall = −0.086, $p = 0.007$), yet their low magnitudes ($|r| < 0.13$) suggest a negligible association. Thus, the two variables can be considered approximately independent for modeling purposes (see SI Fig. S11, SI Text 8.1).

Socioeconomic vulnerability index (SEVI)

The SEVI is the average value of eight socioeconomic components, which are percentile values calculated for each census tract based on the distribution of all values across Pennsylvania. We excluded low-population-density areas when analyzing inundation for different SEVI groups to avoid misleadingly favorable Socioeconomic conditions. The value of the inundation percentage was calculated by dividing the total inundation area in each SEVI group by the total census tract areas in the same SEVI group.

The socioeconomic statistics were analyzed based on the 2010 census block groups rather than the latest 2020 groups to ensure consistency, as specific components still rely on the 2010 census geometries. However, since the latest demographic data is based on 2020 census block groups, we assumed that the population density within the same census tract remains consistent regardless of location. We then recalculated the population density for these mismatched groups using their respective area proportions. This estimate had minimal impact on the detection of low-population areas.

Model validation

The model was challenged and well validated using three methods. First, the overall inundation was qualitatively compared with a single Sentinel-2A MSI Level-2A (atmospherically corrected) image, the only satellite product with acceptable cloud cover during this flooding event. We used the water indices AWEIsh[53] to extract the inundation area and set a 15-cm water depth threshold to consider a wet cell[54] and quantify the inundation area. The "Hit rate" for the DTM and DSM modeling results is 0.51 and 0.68, respectively, indicating positive correspondence. This suggests the model adeptly captures the river channel expansion, even though there is a tendency to overpredict the flood severity, particularly in urban areas. This overprediction aligns with expectations since the model excludes infiltration and drainage networks.

Second, we used the model skill metric (MSM) to assess the model's performance in predicting river discharge and surface elevation[55] (SI Text 3). The MSM s' results consistently exceed 90% (SI Table S1), affirming the model's exceptional ability to reproduce river hydrodynamics accurately.

Last, we used drone images with landmarks to compare the actual inundation extent with the model's predictions. This analysis revealed a strong alignment between the observed and modeled inundation areas, indicating the model's accuracy in representing real-world conditions.

Data availability

River discharge upstream of the Fairmount Dam, at station PA-0147500, is obtained from the USGS water database (https://waterdata.usgs.gov/monitoring-location/01474500/). Tidal elevation downstream is available from a National Oceanic and Atmospheric Administration (NOAA) tide gauge (PA-8543925) (https://tidesandcurrents.noaa.gov/noaatidepredictions.html). Hourly precipitation grids were provided directly by the Office of Hydrological Development, NOAA. 1-meter Digital terrain model (DTM), named as 3D Elevation Program (3DEP), was available from USGS TNM Service (https://apps.nationalmap.gov/downloader/). Newly released LiDAR point cloud data, used to generate Digital Surface Model (DSM), is available from a Philadelphia LiDAR survey (https://geo.btaa.org/catalog/pasda-7154). River bathymetry data was collected from the latest Lower Schuylkill survey provided by the US Army Corps of Engineers Philadelphia (https://www.nap.usace.army.mil/Missions/Civil-Works/Surveys/Projects/). Surface landscape is available from National Land Cover Database (NLCD) 2021 (https://www.usgs.gov/centers/eros/science/national-land-cover-database). Census tracts 2020, the boundary files of districts and watersheds in Philadelphia can be downloaded from Open Data PHLmaps (https://data-phl.opendata.arcgis.com/datasets/). Demographic data on census-tract level is available from 2017-2021 American Community Survey 5-Year Estimates on U.S. Census Bureau (https://data.census.gov/table/). The latest Environmental justice

dataset can be downloaded from PA Department of Environmental Protection (https://gis.dep.pa.gov/PennEnviroScreen/). U.S. Small Business Administration (SBA) dataset loss and loan datasets from 2000 to 2022 are available at https://data.sba.gov/en/dataset/disaster-loan-data. The OpenFEMA dataset of disaster declarations summaries can be downloaded from the official website of the U.S. Department of Homeland Security at https://www.fema.gov/openfema-data-page/disaster-declarations-summaries-v2. The Sentinel-2 satellite image is available from Copernicus Browser (https://browser.dataspace.copernicus.eu/). The road network dataset is available from U.S. Census Bureau, Department of Commerce (https://catalog.data.gov/dataset/).

Code availability

Codes are available at https://doi.org/10.5281/zenodo.17055415[56] to reproduce our results.

Received: 9 December 2025; Accepted: 12 February 2026;
Published online: 25 February 2026

References

1. Zhu, Y.-J., Collins, J. M., Klotzbach, P. J., Schreck, C. J. & Hurricane, I. da (2021): Rapid intensification followed by slow inland decay. *Bull. Am. Meteorol. Soc.* **103**, E2354–E2369 (2022).
2. United Nations University - Institute for Environment and Human Security (UNU-EHS), Higuera Roa, O. & O'Connor, J. *Technical Report: Hurricane Ida*. http://collections.unu.edu/view/UNU:9023 https://doi.org/10.53324/NYKY2894 (2022).
3. Centre for Research on the Epidemiology of Disasters (CRED). *2023 Disasters in Numbers: A Significant Year of Disaster Impact*. https://files.emdat.be/reports/2023_EMDAT_report.pdf (2024).
4. NOAA National Centers for Environmental Information (NCEI). U.S. Billion-Dollar Weather and Climate Disasters. NOAA https://www.ncei.noaa.gov/access/billions/ (2025).
5. IPCC. IPCC, 2023: Climate Change 2023: Synthesis Report. Contribution of Working Groups I, II and III to the Sixth Assessment Report of the Intergovernmental Panel on Climate Change [Core Writing Team, H. Lee and J. Romero (Eds.)]. IPCC, Geneva, Switzerland. https://www.ipcc.ch/report/ar6/syr/ https://doi.org/10.59327/IPCC/AR6-9789291691647 (2023).
6. Zhang, W., Villarini, G., Vecchi, G. A. & Smith, J. A. Urbanization exacerbated the rainfall and flooding caused by Hurricane Harvey in Houston. *Nature* **563**, 384–388 (2018).
7. Jing, R. et al. Global population profile of tropical cyclone exposure from 2002 to 2019. *Nature* **626**, 549–554 (2024).
8. Ghanbari, M., Arabi, M., Kao, S., Obeysekera, J. & Sweet, W. Climate change and changes in compound coastal-riverine flooding hazard along the U.S. coasts. *Earths Future* **9**, e2021EF002055 (2021).
9. Wing, O. E. J. et al. Estimates of present and future flood risk in the conterminous United States. *Environ. Res. Lett.* **13**, 034023 (2018).
10. Sharma, A., Wasko, C. & Lettenmaier, D. P. If precipitation extremes are increasing, why aren't floods?. *Water Resour. Res.* **54**, 8545–8551 (2018).
11. Lopes, C. L. et al. Evaluation of future estuarine floods in a sea level rise context. *Sci. Rep.* **12**, 8083 (2022).
12. Slater, L. J. & Villarini, G. Recent trends in U.S. flood risk. *Geophys. Res. Lett.* **43**, 12428–12436 (2016).
13. Scharf, J. T. & Westcott, T. *History of Philadelphia, 1609–1884*. Vol. 1 (L. H. Everts & Company, Philadelphia, 1884).
14. Interlandi, S. J. & Crockett, C. S. Recent water quality trends in the Schuylkill River, Pennsylvania, USA: a preliminary assessment of the relative influences of climate, river discharge and suburban development. *Water Res.* **37**, 1737–1748 (2003).
15. Gori, A., Lin, N., Xi, D. & Emanuel, K. Tropical cyclone climatology change greatly exacerbates US extreme rainfall–surge hazard. *Nat. Clim. Change* **12**, 171–178 (2022).
16. Balaguru, K. et al. Increased U.S. coastal hurricane risk under climate change. *Sci. Adv.* **9**, eadf0259 (2023).
17. Orton, P. M. et al. Flood hazard assessment from storm tides, rain and sea level rise for a tidal river estuary. *Nat. Hazards* **102**, 729–757 (2020).
18. Jang, J.-H. & Chang, T.-H. Flood risk estimation under the compound influence of rainfall and tide. *J. Hydrol.* **606**, 127446 (2022).
19. Moftakhari, H. R., Salvadori, G., AghaKouchak, A., Sanders, B. F. & Matthew, R. A. Compounding effects of sea level rise and fluvial flooding. *Proc. Natl. Acad. Sci. USA* **114**, 9785–9790 (2017).
20. Teng, J. et al. Flood inundation modelling: a review of methods, recent advances and uncertainty analysis. *Environ. Model. Softw.* **90**, 201–216 (2017).
21. Bates, P. Fundamental limits to flood inundation modelling. *Nat. Water* **1**, 566–567 (2023).
22. Kumar, V., Sharma, K., Caloiero, T., Mehta, D. & Singh, K. Comprehensive overview of flood modeling approaches: a review of recent advances. *Hydrology* **10**, 141 (2023).
23. Sharifian, M. K., Kesserwani, G., Chowdhury, A. A., Neal, J. & Bates, P. LISFLOOD-FP 8.1: new GPU-accelerated solvers for faster fluvial/pluvial flood simulations. *Geosci. Model Dev.* **16**, 2391–2413 (2023).
24. Besse, H. & Rojas-Rueda, D. Environmental justice mapping tools in the United States: a review of national and state tools. *Sci. Total Environ.* **962**, 178449 (2025).
25. Hino, M. & Nance, E. Five ways to ensure flood-risk research helps the most vulnerable. *Nature* **595**, 27–29 (2021).
26. Ohenhen, L. O., Shirzaei, M., Ojha, C., Sherpa, S. F. & Nicholls, R. J. Disappearing cities on US coasts. *Nature* **627**, 108–115 (2024).
27. Ohenhen, L. O. et al. Land subsidence risk to infrastructure in US metropolises. *Nat. Cities* **2**, 543–554 (2025).
28. Josephson, A. & Marshall, M. I. The demand for Post-Katrina disaster aid: SBA disaster loans and small businesses in Mississippi. *J. Contingencies Crisis Manag.* **24**, 264–274 (2016).
29. Collier, B., Howell, S. & Rendell, L. *After the Storm: How Emergency Liquidity Helps Small Businesses Following Natural Disasters*. w32326 http://www.nber.org/papers/w32326.pdf (2024) https://doi.org/10.3386/w32326.
30. Locke, D. H., Roman, L. A., Henning, J. G. & Healy, M. Four decades of urban land cover change in Philadelphia. *Landsc. Urban Plan.* **236**, 104764 (2023).
31. U.S. Geological Survey. *Land Change Monitoring, Assessment*, and Projection (LCMAP). https://pubs.usgs.gov/fs/2020/3024/fs20203024.pdf (2020).
32. Strauss, B. et al. *Pennsylvania and the Surging Sea: A Vulnerability Assessment with Projections for Sea Level Rise and Coastal Flood Risk* https://www.climatecentral.org (2016).
33. Garner, A. J. et al. Impact of climate change on New York City's coastal flood hazard: Increasing flood heights from the preindustrial to 2300 CE. *Proc. Natl. Acad. Sci. USA* **114**, 11861–11866 (2017).
34. Bates, P. Uneven burden of urban flooding. *Nat. Sustain.* **6**, 9–10 (2022).
35. Hoerling, M. et al. Characterizing recent trends in U.S. heavy precipitation. *J. Clim.* **29**, 2313–2332 (2016).
36. Milly, P. C. D. et al. Stationarity is dead: whither water management?. *Science* **319**, 573–574 (2008).
37. Li, A. K. et al. Towards understanding underwater weather events in rivers using autonomous surface vehicles. in *OCEANS 2022, Hampton* Roads 1–8 (IEEE, Hampton Roads, VA, USA, 2022). https://doi.org/10.1109/OCEANS47191.2022.9977236.
38. Slater, L. J., Singer, M. B. & Kirchner, J. W. Hydrologic versus geomorphic drivers of trends in flood hazard. *Geophys. Res. Lett.* **42**, 370–376 (2015).
39. Watson, J. T., Gayer, M. & Connolly, M. A. Epidemics after natural disasters. *Emerg. Infect. Dis.* **13**, 1–5 (2007).
40. Nkwunonwo, U. C., Whitworth, M. & Baily, B. A review of the current status of flood modelling for urban flood risk management in the developing countries. *Sci. Afr.* **7**, e00269 (2020).

41. Tudaji, M., Nan, Y. & Tian, F. Assessing the value of high-resolution rainfall and streamflow data for hydrological modeling: an analysis based on 63 catchments in southeast China. *Hydrol. Earth Syst. Sci.* **29**, 1919–1937 (2025).
42. Hinkel, J. et al. Coastal flood damage and adaptation costs under 21st century sea-level rise. *Proc. Natl. Acad. Sci. USA* **111**, 3292–3297 (2014).
43. Hummel, M. A., Griffin, R., Arkema, K. & Guerry, A. D. Economic evaluation of sea-level rise adaptation strongly influenced by hydrodynamic feedbacks. *Proc. Natl. Acad. Sci. USA* **118**, e2025961118 (2021).
44. Remo, J. W. F., Carlson, M. & Pinter, N. Hydraulic and flood-loss modeling of levee, floodplain, and river management strategies, Middle Mississippi River, USA. *Nat. Hazards* **61**, 551–575 (2012).
45. Jongman, B. Effective adaptation to rising flood risk. *Nat. Commun.* **9**, 1986 (2018).
46. Van Zelst, V. T. M. et al. Cutting the costs of coastal protection by integrating vegetation in flood defences. *Nat. Commun.* **12**, 6533 (2021).
47. Archer, L. et al. Current and future rainfall-driven flood risk from hurricanes in Puerto Rico under 1.5 and 2 °C climate change. *Nat. Hazards Earth Syst. Sci.* **24**, 375–396 (2024).
48. Hatchard, S., Schmitt, R. J. P., Pianosi, F., Savage, J. & Bates, P. Strategic siting and design of dams minimizes impacts on seasonal floodplain inundation. *Environ. Res. Lett.* **18**, 084011 (2023).
49. Soliman, M., Morsy, M. M. & Radwan, H. G. Assessment of implementing land use/land cover LULC 2020-ESRI global maps in 2d flood modeling application. *Water* **14**, 3963 (2022).
50. Martinez-Villalobos, C. & Neelin, J. D. Why do precipitation intensities tend to follow gamma distributions?. *J. Atmosph. Sci.* **76**, 3611–3631 (2019).
51. Goswami, M. Generating design flood hydrographs by parameterizing the characteristic flood hydrograph at a site using only flow data. *Hydrol. Sci. J.* **67**, 2505–2523 (2022).
52. VanderPlas, J. T. Understanding the Lomb–Scargle Periodogram. *Astrophys. J. Suppl. Ser.* **236**, 16 (2018).
53. Yang, X., Qin, Q., Grussenmeyer, P. & Koehl, M. Urban surface water body detection with suppressed built-up noise based on water indices from Sentinel-2 MSI imagery. *Remote Sens. Environ.* **219**, 259–270 (2018).
54. Wing, O. E. J. et al. Validation of a 30 m resolution flood hazard model of the conterminous United States. *Water Resour. Res.* **53**, 7968–7986 (2017).
55. Willmott, C. J. On the validation of models. *Phys. Geogr.* **2**, 184–194 (1981).
56. Xuan, D. & Ulloa, H. N. Compound flood modelling in the Philadelphia-Schuylkill System. Zenodo https://doi.org/10.5281/ZENODO.17478154 (2025).

Acknowledgements

The work was supported by the University of Pennsylvania's University Research Foundation (URF) Award. We greatly acknowledge the support from: the U.S. Army Corps of Engineers Philadelphia District for facilitating the latest sounding survey of the Schuylkill River, the National Weather Service Middle Atlantic River Forecast Center for providing hourly precipitation grids combining rain gauges with radar data. Leandro S. Pongeluppe gratefully acknowledges support from Leonard J. Horwitz, the Wharton Impact, and the Wharton AI & Analytics Initiative. We are grateful to Mark Henninger for generously providing drone images of the flooding triggered by Hurricane Ida in 2021, which were used in this study. We sincerely thank Dr. Jose A. Marengo for valuable scientific discussions related to this study. We thank www.wefilmphilly.com for granting access to the film "The 2021 Philadelphia Flood | Hurricane Ida", which provides rare, event-specific documentation used to benchmark our model against observed flood impacts in Philadelphia.

Author contributions

D.X., H.N.U., M.A.H., D.J.J. designed research, D.X. performed research, H.N.U. supervised research, L.S.P. contributed to economic analysis, M.M.W., M.E.M. contributed to hurricane analysis and discussion; H.N.U. acquired funding; All wrote the paper. All the authors approve the manuscript.

Competing interests

The authors declare no competing interests.

Additional information

Supplementary information The online version contains supplementary material available at https://doi.org/10.1038/s44304-026-00186-8.

Correspondence and requests for materials should be addressed to Dingyu Xuan or Hugo N. Ulloa.

Reprints and permissions information is available at http://www.nature.com/reprints

Publisher's note Springer Nature remains neutral with regard to jurisdictional claims in published maps and institutional affiliations.

Open Access This article is licensed under a Creative Commons Attribution 4.0 International License, which permits use, sharing, adaptation, distribution and reproduction in any medium or format, as long as you give appropriate credit to the original author(s) and the source, provide a link to the Creative Commons licence, and indicate if changes were made. The images or other third party material in this article are included in the article's Creative Commons licence, unless indicated otherwise in a credit line to the material. If material is not included in the article's Creative Commons licence and your intended use is not permitted by statutory regulation or exceeds the permitted use, you will need to obtain permission directly from the copyright holder. To view a copy of this licence, visit http://creativecommons.org/licenses/by/4.0/.

© The Author(s) 2026

Supplementary Information

for

Climate extremes and urbanization drive flood tipping points at the city–river interface

Dingyu Xuan[1,2], M. Ani Hsieh[3,4], Leandro S. Pongeluppe[5], Mackenzie M. Weaver[1], Michael E. Mann[1], Douglas J. Jerolmack[1,4], Hugo N. Ulloa[1]

[1]Department of Earth and Environmental Science, University of Pennsylvania, Philadelphia, US

[2]Department of Civil and Environmental Engineering, Imperial College London, London, UK

[3] Department of Computer and Information Science, University of Pennsylvania, Philadelphia, US

[4] Department of Mechanical Engineering and Applied Mechanics, University of Pennsylvania, Philadelphia, US

[5] Wharton School, University of Pennsylvania, Philadelphia, US

Supplementary Text 1: LISFLOOD-FP Model Description

LISFLOOD-FP serves as the hydraulic engine to resolve rainfall-, topographic-, and tidally-driven hydrodynamics of channel and floodplain flows. It provides a wide range of solvers to deal with flows from different dimensions[1–6]. In our study, we used a latest updated numerical solver, acceleration solver (ACC)[6], to simulate river dynamics and map water pathways. This modeling framework will incorporate extensive geographical and weather data, including meteorological, urban, marine, and new underwater observations[7]. The depth-averaged mass and momentum equations for this solver can be written in Cartesian coordinates $(x,\, y,\, z)$ as

$$\overbrace{\frac{\partial h}{\partial t} + \frac{\partial q_x}{\partial x} + \frac{\partial q_y}{\partial y} = r}^{\text{Mass conservation}}, \tag{1}$$

$$\overbrace{\frac{\partial q_x}{\partial t} + \frac{\partial}{\partial x}\left(\frac{q_x^2}{h}\right) + \frac{\partial}{\partial y}\left(\frac{q_x q_y}{h}\right)}^{\text{Rate of change momentum in } x-\text{direction}} = \overbrace{-g\frac{\partial}{\partial x}\left(\frac{h^2}{2}\right) - gh\frac{\partial z}{\partial x} + \frac{g\, n^2 |q_x| q_x}{h^{7/3}}}^{\text{Sum of forces in } x-\text{direction}}, \tag{2}$$

$$\overbrace{\frac{\partial q_y}{\partial t} + \frac{\partial}{\partial x}\left(\frac{q_x q_y}{h}\right) + \frac{\partial}{\partial y}\left(\frac{q_y^2}{h}\right)}^{\text{Rate of change momentum in } y-\text{direction}} = \overbrace{-g\frac{\partial}{\partial y}\left(\frac{h^2}{2}\right) - gh\frac{\partial z}{\partial y} + \frac{g\, n^2 |q_y| q_y}{h^{7/3}}}^{\text{Sum of forces in } y-\text{direction}}, \tag{3}$$

where h is the water depth; t is the time; q_i represents the flow discharge per unit width, with subscript $i = x,\, y$ in the Eq. 1–3 indicating flow component in the x and y direction; the precipitation rate, r, is treated as a mass flux in Eq. 1; g is the gravitational acceleration; n is the Manning friction coefficient; and z is the landscape elevation coordinate pointing upward. The terms on the left-hand side of Eq. 2 and Eq. 3 represent the acceleration of the flow caused by the forces acting on the water. The first, second and third terms in the right-hand side of Eq. 2 and Eq. 3 are the forces exerted by the horizontal pressure gradient, the gravity force and viscous drag force acting in the water, respectively.

The numerical schemes of the solver can handle source and sink terms, enabling the modeling of spatially and temporally varying processes like precipitation and local water discharges. Momentum change results from pressure, gravity, and frictional forces, parameterized with space-dependent Manning coefficients. Unlike many CPU-based solvers, LISFLOOD-FP can run on NVIDIA GPU cores[5;6], significantly enhancing computational efficiency for high-resolution modeling (e.g., 1 meter resolution) that captures flows through narrow city pathways. Its robustness and accuracy with real inundations have been demonstrated[8;9].

Supplementary Text 2: Watershed Elevation

Surface elevation Generation. This model utilizes an accurate Digital Surface Model (DSM) generated from Light Detection and Ranging (LiDAR) point cloud data collected on March 29, 2022, including urban landscape surrounding the Schuylkill River (buildings, streets, and canopies). In contrast, the DTM, obtained from 3DEP at one-meter resolution, ignores human-made infrastructures. Both elevation models were adjusted to NAD83 UTM horizontal and NAVD88 vertical datums for consistency. To balance capturing details and computational efficiency, spatial resolution for both landscape models was resampled to 5 m, enough to resolve the flow at the street level. All sinks in both elevation data were first filled by ArcGIS before detecting flow directions, allowing more accurate representation of flood propagation.

River bathymetry. Accurate riverbed elevation data from bathymetric surveys is crucial for improving the precision of fluvial flood modeling, as microwaves and typical radars on satellites cannot penetrate water[10]. We obtained bathymetric points for the lower Schuylkill River from surveys conducted by the US Army Corps of Engineers, covering both upstream and downstream regions of the Fairmount Dam. Interpolation methods are employed to create a continuous model of river bathymetry, and the choice of methods significantly impacts the robustness of the underwater landscape representation[11;12]. Upstream bathymetric points were distributed along cross-sections, while those around and downstream of the dam were heterogeneously spaced (see Fig. **S3**). Based on the point distribution and performance tests, we applied the Original Kriging method downstream of the dam, given its high accuracy in densely measured areas[11], and used the Natural Neighbor method to interpolate observations upstream. Additionally, a "3x3 cells area" low filter window was applied to the DEM to smooth abrupt elevation differences along the flow direction.

Supplementary Text 3: Modeling Validation

In our study, calculated inundation areas excluded existing water bodies, such as the Schuylkill River surface under normal conditions. Since all cells in the domain contained some water once rainfall was included in the model, a 15-cm water depth threshold was applied to define wet cells (i.e., cells are considered inundated when water depth exceeded 15 cm)[13].

We further used the model skill metric (MSM) to assess the modeling performance of the river discharge and surface elevation, with the equation given below:

$$MSM = 1 - \frac{\sum |x_m - x_o|^2}{\sum (|x_m - \overline{x}_o| + |x_o - \overline{x}_o|)^2} \tag{4}$$

where x_m is the model result, x_o is the observation data, and $\overline{x}_o$ is the average value. MSM close to 1 indicates a better fit between the model and the observation. The MSM values for each cross section and elevation model were presented in Table **S1**.

Supplementary Text 4: Economic and Financial Analysis

Data description and uncertainties. The SBA dataset originates from the U.S. SBA's Disaster Loan Program and includes only anonymized, non-personally identifiable information. The program provides post-disaster financial support through affordable, long-term loans to businesses, nonprofit entities, homeowners, and renters for damages that are not otherwise compensated by insurance or alternative recovery resources.[14]. The dataset includes verified loss data—total, real estate, and personal property (content)—as well as approved loan amounts for real estate, content, and Economic Injury Disaster Loan (EIDL) assistance. The available dataset covers the period from 2000 to 2022. For some year such as from 2019 onward, the SBA recorded verified losses and approved loans separately for home and business categories, while other years (especially in earlier years), only the combined total were reported. To ensure consistency across the full time series, we aggregated the home and business data for recent years to obtain comparable total loss and loan amount.

The verified loss for real estate is the verified dollar amount of physical damage to buildings or real property (for instance, a home, business premises). The verified loss for content is the verified amount of damage to personal property or business contents, such as furniture, inventory, and equipment. The total verified loss is the sum of real estate and content losses. The approved loan for real estate is the portion of the approved SBA disaster loan allocated for repairing or replacing real estate, while the approved loan for content is the portion for personal property. The approved EIDL loan is the approved amount for economic injury that intended to help small businesses cover working capital losses caused by the disaster, for example, lost revenue while closed[14].

Each record has assigned declaration numbers. The FEMA disaster number is a unique identifier assigned to a specific, federally declared disaster, such as a hurricane, earthquake, or flood. The SBA Disaster Number tracks SBA disaster loan declarations, which could be independent or tied to a FEMA disaster. The SBA can issue its own declaration when a governor certifies that at least 25 homes or businesses have sustained major damage or destruction, and no federal FEMA disaster is declared. That's why each event recorded in the SBA dataset has an SBA Disaster Number but no corresponding FEMA number.

However, the SBA Disaster Loan dataset contains several sources of uncertainty that may affect data reliability. First, since entries are manually entered, they are subject to human error and incompleteness. Second, the dataset is periodically updated, but early estimates may

not be revised, introducing uncertainty in time-based analyses. Third, loan amounts can be influenced by overlaps with other assistance programs—such as insurance or grants—which may lead to bias or duplication. Fourth, dollar values are reported in nominal terms without inflation adjustment, making cross-year comparisons sensitive to changes in purchasing power. Finally, the dataset covers only SBA loan recipients, leading to potential sample bias, as it does not represent all affected individuals or households. Overall, these factors imply that the dataset should be interpreted as an approximate indicator of disaster losses and recovery support rather than an exact financial accounting[14].

Data preprocessing. We downloaded the SBA datasets and the OpenFEMA *Disaster Declarations Summaries* Dataset[15] to identify FEMA disaster numbers associated with Hurricane Ida. Three declaration titles were found to be relevant: Remnants of Hurricane Ida, Hurricane Ida, and Tropical Storm Ida. The detailed list of corresponding FEMA disaster numbers and the associated states is presented in Table **S2**. The records were further filtered by declaration year (starting from 2021) and by disaster type, limited to floods, storms, or hurricanes. Two key dummy variables were then constructed for the analysis: (1) *is_philadelphia_zip*, indicating whether the declaration occurred in Philadelphia (=1) or not (= 0); and (2) *ida_zip_year*, indicating whether the record corresponds to the 2021 Ida event (= 1) or not (= 0). When assigning the *ida_zip_year* variable, we restricted the potentially affected states to those located directly along Ida's path or in the neighboring states, to avoid misclassifying records from distant regions. Next, relevant records were extracted based on these two variables, including all declarations where either *is_philadelphia_zip* = 1, or *ida_zip_year* = 1, or both. The resulting dataset was grouped by key geographic identifies (e.g., zip code, county, and state), and all relevant loss and loan variables were aggregated annually for each region.

Econometric estimation. Similar to other studies on related topics[16;17], we used the SBA disaster loan data. We followed the quasi-experimental literature[18;19] and estimated a Difference-in-Differences (DiD) model to identify the local additional economic impact of Hurricane Ida on Philadelphia, considering verified losses and approved disaster loans. The unit of observation is the zipcode-year pair, the most fine-grained geographical level we were able to operationalize. Formally, the econometric estimations follow the model:

$$Y_{i,t} = \beta_1(\mathrm{Ida}_{i,t} \times \mathrm{Philadelphia}_i) + \beta_2\,\mathrm{Ida}_{i,t} + \beta_3\,\mathrm{Philadelphia}_i + \gamma\,X_{i,t} + \delta_i + \gamma_t + e_{i,t} \quad (5)$$

where $Y_{i,t}$ denotes the outcome variables for each zipcode i in year t. The primary outcome variables in our analyses are the Total Verified Loss (USD) and the Total Approved Loan Amount (USD) presented in Panel A, Tables **S3** and **S4**. We also performed analy-

ses, breaking down each outcome by Verified Loss Real Estate (USD) and Approved Amount Real Estate (USD) in Panel B, Tables **S3** and **S4**, and by Verified Loss Content (USD) and Approved Amount Content (USD) in Panel C, Tables **S3** and **S4**, with "Content" defined by SBA as personal property, auto, etc. "$\mathrm{Ida}_{i,t}$" is a dummy variable taking the value of 1 in years that a zipcode affected by Hurricane Ida requested support from SBA for damages related to the Hurricane Ida disaster, and 0 otherwise. In within-city models (Columns 1, 4, and 7 in Tables **S3** and **S4**), this variable shows the effect of the hurricane in zip codes affected by Ida, comparing them with other zip codes within Philadelphia, but that did not report damages related to Hurricane Ida. "$\mathrm{Philadelphia}_i$" is a dummy variable taking the value of 1 for zipcodes located in the Philadelphia metropolitan area and 0 otherwise. $(\mathrm{Ida}_{i,t} \times \mathrm{Philadelphia}_i)$ captures the additional effect of the hurricane on Philadelphia relative to other zipcodes within the state of Pennsylvania (Columns 2, 5, and 8), or within all affected states (Columns 3, 6, and 9). $X_{i,t}$ is a control variable, based on the total number of records requesting support for a given zipcode in a given year. This variable aims to control for the intensity of the effect on a particular zipcode. δ_i and γ_t are zip code and year fixed effects, respectively, which aim to correct for all zipcode-specific time-invariant characteristics, and for year-specific shocks. Finally, $e_{it,}$ is the error term of the regression. Models have standard errors clustered at the zip code level to account for serial correlation within zip code geographic areas[20].

Our preferred estimation is the within-Pennsylvania models (Columns 2, 5, and 8) since the within-state comparison allows us to properly compare locations under the same legal and political jurisdiction. This specification avoids biases from potential spillover between affected and unaffected zip codes in within-city models, and from an inadequate composition of the control group in within all-affected states models. We report all models for transparency. Therefore, β_1 is the coefficient estimate of interest, which measures the average additional verified loss or approved loan amount in Philadelphia attributable to Hurricane Ida, relative to other areas in the same state (Columns 2, 5, and 8). These estimates are reported in Tables **S3** and **S4**.

Financial valuation analysis. We used the coefficient estimates β_1 from the within-state econometric analysis to assess the financial implications of Hurricane Ida. Specifically, we constructed a simplified cash flow model to estimate the net present value (NPV) of the disaster's impact on Philadelphia, incorporating both losses and credit-based relief[21].

For each zipcode i, we defined the incremental net cash flow at present value, i.e., the disaster year following the model:

- **Initial shock**: at time $t = 0$, society bears the costs of both the direct property losses from the disaster and the SBA loan disbursements, which have to be provided by the government:

$$CF_i^0 = -\beta_1^{Loss} - \beta_1^{Loan} \tag{6}$$

- **Grace period**: SBA loans have a grace period of 12 months (i.e., $t = 1$), so no repayment occurs during this period:

$$CF_i^1 = 0 \tag{7}$$

- **Repayments**: From years $t = 2, \ldots, 31$, SBA receives loan repayments from approved borrowers who do not default. We assume SBA's annual interest rate to borrowers is subsidized and, on average, equals to $i_L = 0.02 \sim 2\%$ and a loan term $T = 30$ years, which is consistent with information found on SBA's webpage[22]. Thus, the annual repayment equals P, such that:

$$P = \left[\beta_1^{Loan} \times \frac{i_L}{1 - (1 + i_L)^{-T}} \right] \tag{8}$$

- **Defaults**: Since some proportion of borrowers might not be able to recover from the disaster even with the governmental loan, we attribute a default rate $d \in \{0\%, 10\%, 20\%\}$, the expected inflow of repayments each year is:

$$CF_i^t = (1 - d)P, \; t = 2, ..., 31 \tag{9}$$

- **Net Present Value**: The $NPV_i\,(r, d)$ for the average zipcode i, the formula below follows, varying the discount rate $r \in \{1\%, 5\%, 7\%, 9\%, 11\%\}$ for sensitivity analysis, since the amount allocated to the loans could be directed to alternative investments with varying rates of return:

$$NPV_i\,(r, d) = \sum_{t=0}^{T=31} \frac{CF_i^t}{(1 + r)^t} \tag{10}$$

  Given that a total of 126 zipcodes were affected by Hurricane Ida in Philadelphia, Z=126. Thus, the whole Philadelphia NPV is:

$$NPV\ Total\ (r, d) = NPV_i \times Z \tag{11}$$

The results of this valuation model suggest that across all parameter combinations, the estimated $NPV\ Total\ (r, d)$ remains consistently negative, ranging from USD 19.9 to USD 21.4 million, indicating substantial net welfare loss (Fig. **S4** and Table **S5**).

Final remarks and limitations. These models focus exclusively on verified property losses and disaster loans. They do not include broader economic costs such as higher insurance premiums, healthcare expenses, lost labor income, permanent business closures, or fatalities. Consequently, the estimated NPVs represent a conservative lower bound on the overall

economic cost of Hurricane Ida to Philadelphia.

Supplementary Text 5: Runoff Analysis

Surface runoff coefficient. The surface runoff coefficient measures the proportion of rainfall that is converted to surface runoff during a hydrological event, reflecting the land's capacity for infiltration and water storage. The detailed equation is provided below:

$$\mathcal{C} = \frac{\Delta\, Q}{k\, A\, (R_{\mathrm{cum}}/T_{\mathrm{cum}})} \tag{12}$$

where $\Delta\, Q\ (\mathrm{m^3 s^{-1}})$ indicates the increase in river discharge at each peak; k is a coefficient for unit conversion (here k = 0.278); $A\ (\mathrm{km^2})$ is the area of the upstream watershed (i.e. 4862.504 $\mathrm{km^2}$); $R_{\mathrm{cum}}\ (\mathrm{mm})$ and $T_{\mathrm{cum}}\ (\mathrm{h})$ are the cumulative rainfall value and overall rainfall time before each peak, respectively.

Frequency analysis for river discharge. A return period (RP) is the reverse of an exceedance probability. The exceedance probability of a river is related to the likelihood that a certain river discharge will be exceeded in any given year. We collected annual peak river flows from 1931 to 2024 and sorted them in a decreasing order, and then defined RPs based on the following equation:

$$P_{\mathrm{i}} = \frac{m}{n+1} \tag{13}$$

where P_{i} is the exceedance probability for the i-th discharge; m is the rank of the discharge, with the highest value having m = 1; n is the total number of discharge values in the dataset, and "+1" leaves the space for a full probability with a small number of datasets. Here, n = 94. We assumed that the highest value in this 94-year-RP river series closely approximates the 100-year-RP, so we used the latter term in our paper for simplicity. The analyses for every two decades were just the same, but the RP should be re-calculated based on each 20-year time series, which affects the rank of the discharge m in Eq. 13.

Tidal impact on river discharge. The interpolated smooth tidal elevation series was used as the downstream boundary for the study region. As shown in Fig. **S6**b-c, upstream sections above the dam ($A1$ and $A2$) show no tidal impact, while downstream sections ($B1 - B3$) exhibit clear tidal signals during low-flow periods, regardless of the elevation model used. This indicates that the Fairmount Dam block tidal propagation upstream, thereby reducing saline intrusion to upstream regions under normal conditions, though its barrier effect weakens during extreme events. Urbanization is also expected to increase river discharge during extremes (Fig. **S6**d), likely because leeves or embankments along the banks confine flow within the

channel, raising water levels, whereas natural channels typically spread laterally and dissipate momentum at high discharges.

Standardized hydrograph detection. We used long time series of river discharge, from 1931 to 2024, to better understand the single-peaked hydrograph of the Schuylkill River, thereby designing flood hydrographs of more severe scenarios. The original hydrographs from observation were shown in Fig. **S7**a. The 2021 flood event, as simulated above, has a 100-year return period, indicating that this event is the most serious fluvial flood event on record. All hydrographs were then standardised to analyse their shapes (Fig. **S7**b). Two equations based on the gamma distribution and exponential function were used to fit the rising and recession limb of the hydrograph[23]:

$$Q = \left(\frac{t + t_0}{t_0}\right)^{m-1} \exp\left(-\frac{t(m-1)}{t_0}\right) \tag{14}$$

$$Q = q_s \exp\left(-\frac{t - t_s}{n}\right) \tag{15}$$

where Q is the river discharge; t shows the time value, t_0, as a location parameter, is the time duration before peak; m and n are shape parameters; and (t_s, q_s) is the starting point of Eq. 15. This point is better set at the inflection point of the recession limb rather than just at the peak point, which is the same as what[23] suggested. In this study, t_0 = 25, m = 7.5, n = 11, and the starting point is (8, 0.7). The results were shown in Fig. **S7**c.

Supplementary Text 6: Tidal Analysis

Spectral density and harmonic analysis. Local tidal observations report only the highest and lowest surface water levels with their associated times. For this unevenly spaced time series, we applied a Lomb-Scargle periodogram to identify the dominant tidal frequencies and periods[24] (Fig. **S8**a-b). The four strongest constituents detected were then used as initial guesses in a harmonic analysis, which interpolated the discrete observations (August 23 - September 10, 2021) into a smooth curve of tidal elevations (Fig. **S8**c). The harmonic analysis showed a good fit to the observation data, with a root mean square error (RMSE) of 0.084 m.

Characteristics of tidal constituents. The results of harmonic analysis reveal that four principal tidal constituents primarily influence the Lower Schuylkill: the semidiurnal lunar tides M_2 = 12.42 h, the semidiurnal solar tide S_2 = 12.00 h, and the diurnal tides K_1 = 23.92 h and O_1 = 25.88 h. The detailed values for the amplitude, period, and phase of these tidal components were presented in Table **S7**.

When tidal elevations above and below the dam are plotted over a fortnightly cycle in two dimensions, clear daily and weekly shifts in tidal levels are evident (Fig. **S9**a). Downstream, tidal signals in river discharge become increasingly distinct with distance from the dam (Fig. **S9**c-d), showing an around 4-hour lag between daily peak tide and peak discharge at the downstream boundary.

Supplementary Text 7: Sediment Analysis

Sediment concentration datasets for the Schuylkill River were obtained from the USGS river station (PA-01474500). Data availability is limited to the years 1959 to 1968, and even within this period, there are significant gaps. In total, approximately 5 years of usable data are available for analysis. Although river discharge appears to be positively correlated with sediment concentration (Fig. **S10**a-c), sediment mobilization is governed by bed shear stress rather than discharge alone[25]. Therefore, both shear stress and river discharge were plotted against sediment concentration to visualize their relationships (Fig. **S10**d-i). The bank-full shear stress (τ) is calculated using the following equation[25]:

$$\tau = \rho g H S \tag{16}$$

where ρ is fluid density (assumed equal to water density, $\rho = 1000\ \mathrm{kg/m^3}$), g is gravitational acceleration (9.81 $\mathrm{m/s^2}$), H is the channel-average bank-full flow depth, and S is the energy slope (approximated as the channel bed slope for uniform flow). Since the station is located upstream of the dam, the flow rate is generally low and both the water surface and bed slope are nearly flat. Thus, S is assumed to be 0.01.

Gage height data for this station is only available post-2007 and therefore does not overlap with the period of sediment concentration measurements. However, a widely-accepted power-law relationship exists between river depth (d) and discharge (Q)[26;27]:

$$d = aQ^b \tag{17}$$

We used available discharge and gage data from 2007 to 2025 to tailor this empirical relationship to the Schuylkill River. It is important to note that the USGS provides gage height, not direct river depth. Thus, gage values were converted to river depth using the following conceptual equation:

$$\text{river depth} = (\text{gage datum} + \text{gage height}) - \text{river bed elevation} \tag{18}$$

The gage datum used by USGS is based on the NAVD88 vertical reference, and the gage

station is 4.54 ft (around 1.38 m) above the reference level. The river bed elevation near the station, estimated from recent bathymetry surveys, is approximately 0.96 m. Using this information, we derived a revised depth-discharge function specific to the site:

$$d = 1.73(Q - 34.40)^{0.05} + 0.01(Q - 34.40)^{0.74} \tag{19}$$

This equation achieved a root mean square error (RMSE) of around 0.01 m between observed and predicted depths. The estimated depths were then applied to Eq. 16 to calculate bed shear stress near the station. Overall, sediment concentration increases markedly when bed shear stress exceeds 24 Pa, with a positive correlation observed between stress magnitude and sediment levels (Fig. **S10**d-f).

Supplementary Text 8: Scenario Modeling

Independency analysis between tides and discharge. Before analyzing the combined effects of tidal levels and river discharge on flood inundation, it is essential to first examine their dependency. In particular, is it physically plausible for a river peak to coincide with a low tidal level? We used Spearman's correlation coefficient to measure the correlation between upstream river discharge and downstream tidal levels. All data in each dataset was first ranked in an ascending order and input to the equation as followed[28]:

$$r_s = 1 - \frac{6}{n(n^2 - 1)} \sum_i d_i^2, \tag{20}$$

where n is the number of data in the dataset; d_i is the ranking difference between two datasets. r_s has a value ranging from 0 to 1, with a higher value representing a higher correlation. The correlation analysis shows only a minimal association between the two (Fig. **S11**a). The central hexbin plot (Fig. **S11**b) further illustrates a scattered distribution, suggesting that upstream peak river discharge and downstream tidal elevation are largely independent. In practice, high river discharge can occur during either low or high tides. This independence underpins the tidal scenario design used in our subsequent analysis.

Impact of rainfall and tidal phases on inundation area for Ida's flood. We defined tidal phases (TP$\in [0, 1]$) regarding to half of a semi-diurnal cycle, which represent the time-lag between the tide amplitude of the dominant constituent and the peak in river discharge. The range $0.0 < TP \leq 0.5$ is associated with a rising tide amplitude, with $TP = 0.5$ indicating the phase at which the highest tide amplitude aligns with the peak in river discharge. In contrast, the range $0.5 < TP \leq 1.0$ is associated with a falling tide amplitude. The elevation for different

TPs is selected from the semi-diurnal tide during the peak of the 2021 flood hydrograph (see the red highlighted block in Fig. **S9**a).

To evaluate the impact of tides on compound flood risk, we measured the inundation area as a function of the tidal phase, incorporating the rainfall pattern cast by Hurricane Ida into our model. Yet, disentangling the effect of tides in the Philadelphia urban landscapes is complicated as surface flow patterns are case specific, complex to predict, and often obstructed by human infrastructure. This leads us to the following question: how far can the tide signal penetrate into the city and influence the compound flood event? To address this, we concentrate our analysis into the river and examine the inundation patterns within a buffer zone. The analysis reveals that tidal phase affects maximum river flood inundation, with inundation area increasing when peak discharge coincides with higher tidal levels (Fig. **S12**a). The worst-case tidal scenario is when the river flood wave faces the King tide, as it raises water levels in the Lower Schuylkill and hinders the river's ability to drain into the Delaware River.

How does rainfall affect the flooding in the tidally controlled buffer zone? Our results show that this effect depends on tidal phases. In fact, tides periodically shrink and enlarge the volume available to absorb both river and rainfall input in the estuarine zone. Therefore, depending on the timing of rainfall and river peaks relative to the tide amplitude, the actual contribution to flooding can vary significantly (Fig. **S12**a). Fig. **S12**b illustrates the actual increase in flood area due to rainfall across different tidal phases. We note that during low tide conditions ($TP = 0.25$), rainfall leads to the largest inundation area within the 100-meter buffer zone. Conversely, during $TP = 0.42$ (as observed during Hurricane Ida), the near maximum tide amplitude leaves less space for rainfall input to contribute to the buffer zone flooding. In this case, the increase in inundation area is primarily driven by the river peak, which penetrates through Philadelphia's most densely populated neighborhood[29].

To quantify the impact of tides on inundation patterns for compound flood events, we used Spearman's correlation coefficient to measure the correlation between the inundation patterns (dataset X) and a semi-diurnal signal of the Schuylkill River (dataset Y). Sensitivity analyses show that within a 100-m buffer zone (approximately a block from the riverbank), tides strongly modulate the flood extent for a river discharge of 100-year-RP, with a tidal correlation value exceeding 0.9 (Fig. **S12**c). However, as the buffer distance is further extended, the influences of tides gradually diminished, becoming negligible at around 200 to 250 meters from the riverbank, with the correlation decreasing to around 0.8. Beyond this boundary, rainfall dominates inundation patterns. As the buffer width expands, the "tidal-like" patterns in flood inundation gradually weaken and disappear about 500 m from the bank in the Lower Schuylkill River, as increasing rainfall-driven flood "noise" enters the inundated distribution. In this study, the focus is on the interaction between river discharge and tides, while predicting future rainfall patterns would require large-scale meteorological models beyond the scope of this work. The

combined rainfall-river-tide dynamics is more complex and needs further investigation.

Impact of RP river flows and tidal phases on river flood inundation We focused on river dynamics to assess how tides affect even more extreme events with higher RPs. As upstream flows are intensified to higher RPs, the tidal pattern on river inundation persists, but with an offset in the TP associated with maximum inundation. The shift occurs when the peak tide aligns with the rising limb of the river hydrograph, such as at TP = 0.38 for a 5000-year-RP inflow (Fig. **S13**a). This is because maximum inundation is reached when downstream tidal forcing balances upstream flows. In the downstream Schuylkill, tides consist of four primary modes. A diurnal tide can alter the semi-diurnal amplitude within its diurnal cycle, so the amplitudes of the peak in adjacent semi-diurnal cycles are different (Fig. **S13**b). When TP gets smaller, the whole tidal series are shifted rightward visually, allowing the higher-peaking semi-diurnal tide to counter the river's rising limb more effectively. This resistance effect increases with higher river inflows, resulting in a greater river flood inundation. Thus, while peak river flood inundation continues to coincide with the King tide, worst-case scenario should also take the TP into account.

As river discharge increases, the TP associated with maximum inundation tends to occur earlier, reflecting an earlier balance point between riverine and tidal forces. Yet, the hydrograph typically spans more than a week and incorporates multiple tidal waves and peaks. Since we found that tidal peaks aligning with the rising limb of the hydrograph can lead to higher inundation as river inflow increases, the combined effect of all tidal peaks needs careful consideration when analyzing the entire hydrograph in future studies (Fig. **S13**).

Supplementary Figures

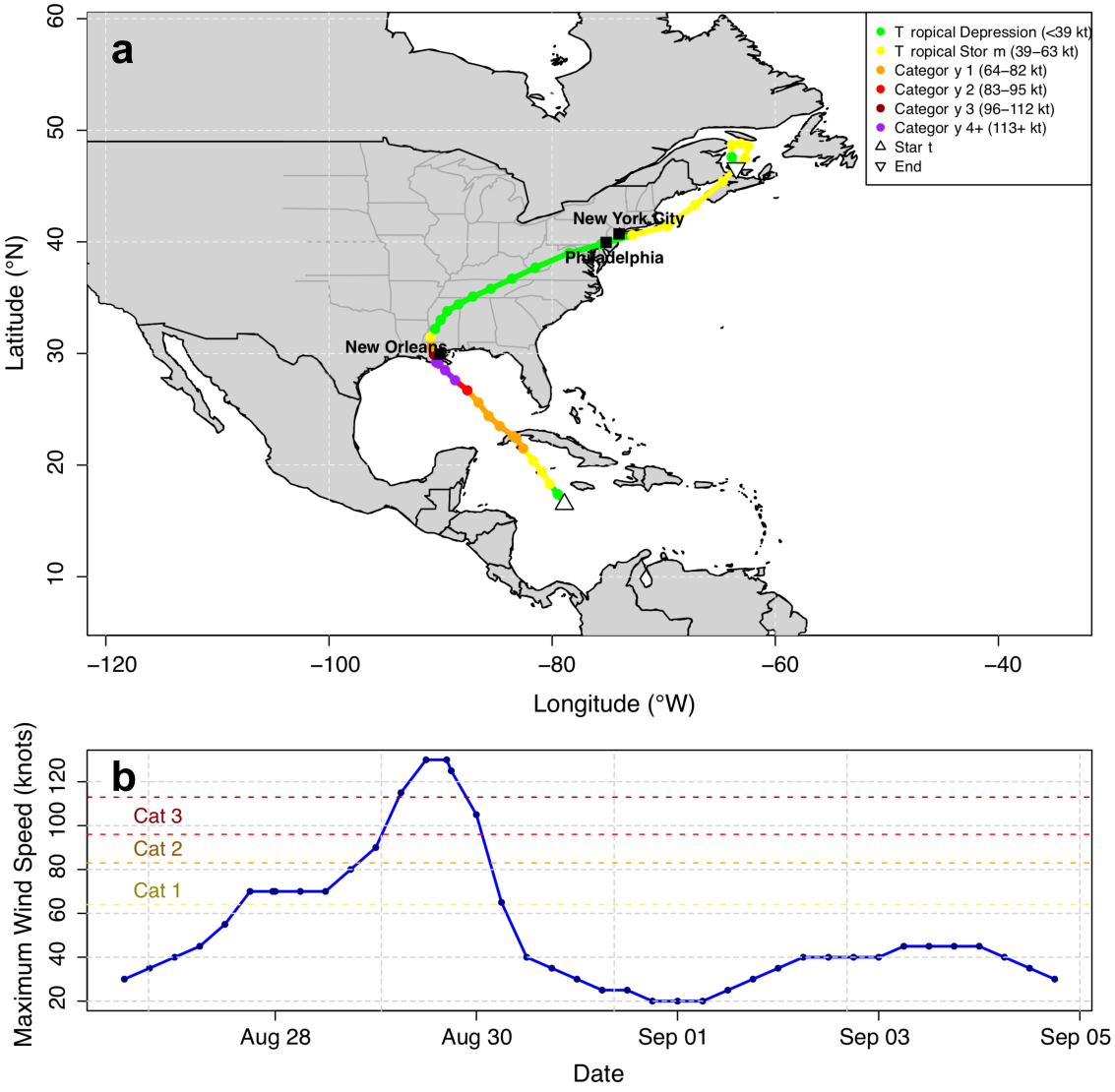


Fig. S1: Overview of Hurricane Ida. (a) The trajectory of Hurricane Ida, originating in the Gulf of Mexico, making landfall near New Orleans, and continuing northward through Philadelphia and New York. (b) Temporal variation in Ida's intensity, represented by changes in maximum wind speed.

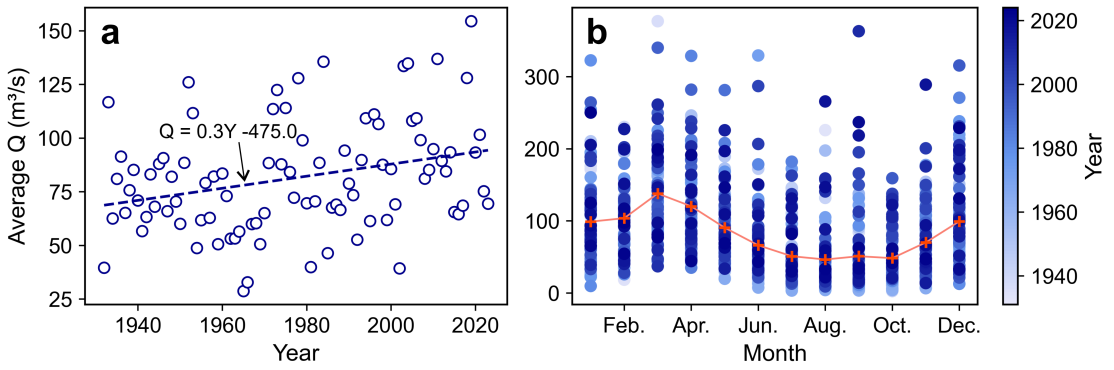


Fig. S2: Hydrological regime of Schuylkill River. This figure is adapted from Fig. 1 in[30], with the dataset extended by over 20 years for analyzing the current status. (a) Annual average river discharge of the downstream Schuylkill River from 1932 to 2023. The flow data was collected from USGS gauge station, PA - 01474500. The dash line indicates the overall trend of annual discharge with a positive gradient. (b) Monthly average river discharge at the same station from 1932 to 2023. Red markers show the average flow value within each month.

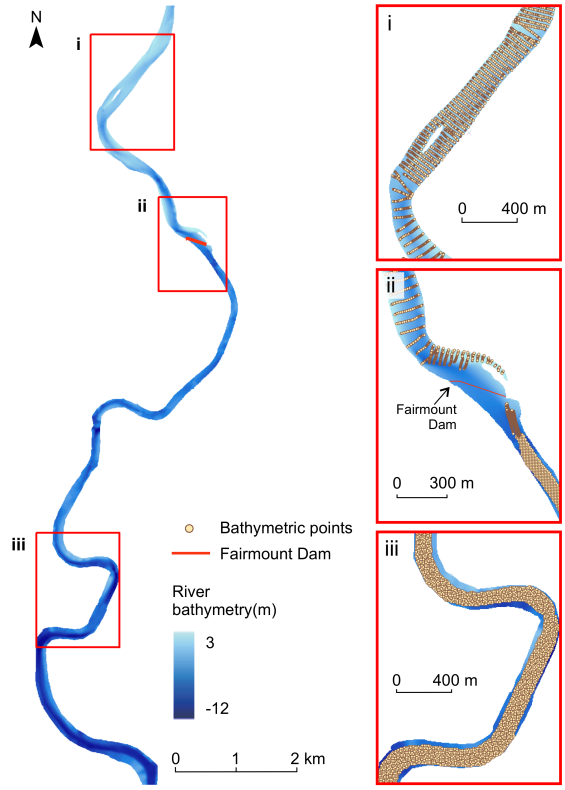


Fig. S3: Different spatial patterns of bathymetric points and the river bathymetry after interpolation. (i) Points above the dam, (ii) around the dam, and (iii) below the dam. The dam serves as a boundary for data collection methods: above the dam, points are collected across river sections, whereas below the dam, they are spaced heterogeneously.

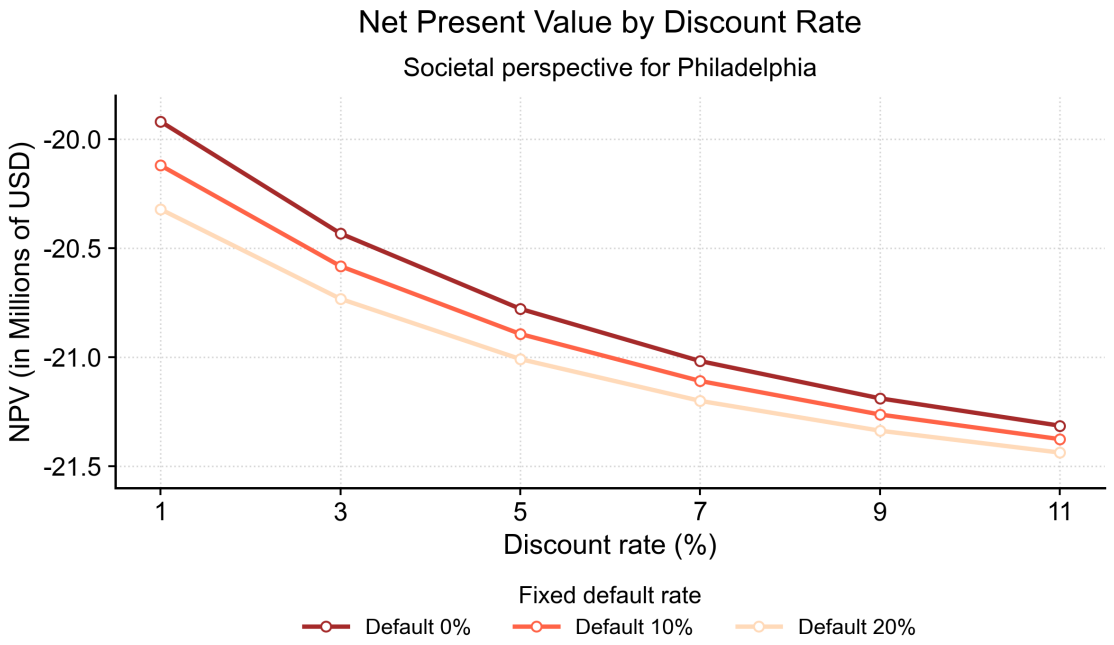


Fig. S4: Net present value (NPV) by discount rate, as a societal perspective for Philadelphia. Considering additional loss in Philadelphia (ΔLoss=160,061); Additional loan in Philadelphia (ΔLoan=13,997); SBA average interest rate (APR iL = 2%); SBA 12-month grace period; 30-year amortization. $\mathrm{CF}_0 = -\Delta\ \mathrm{Loan} - \Delta\ \mathrm{Loss}$; $\mathrm{CF}_1 = 0$; $\mathrm{CF}_\mathrm{t} = (1-p)P$ from t = 2 to t = 31 year; $\mathrm{P} = \Delta\ \mathrm{Loan} \cdot\ \mathrm{iL}/[1-(1+\mathrm{iL})^{-30}]$.

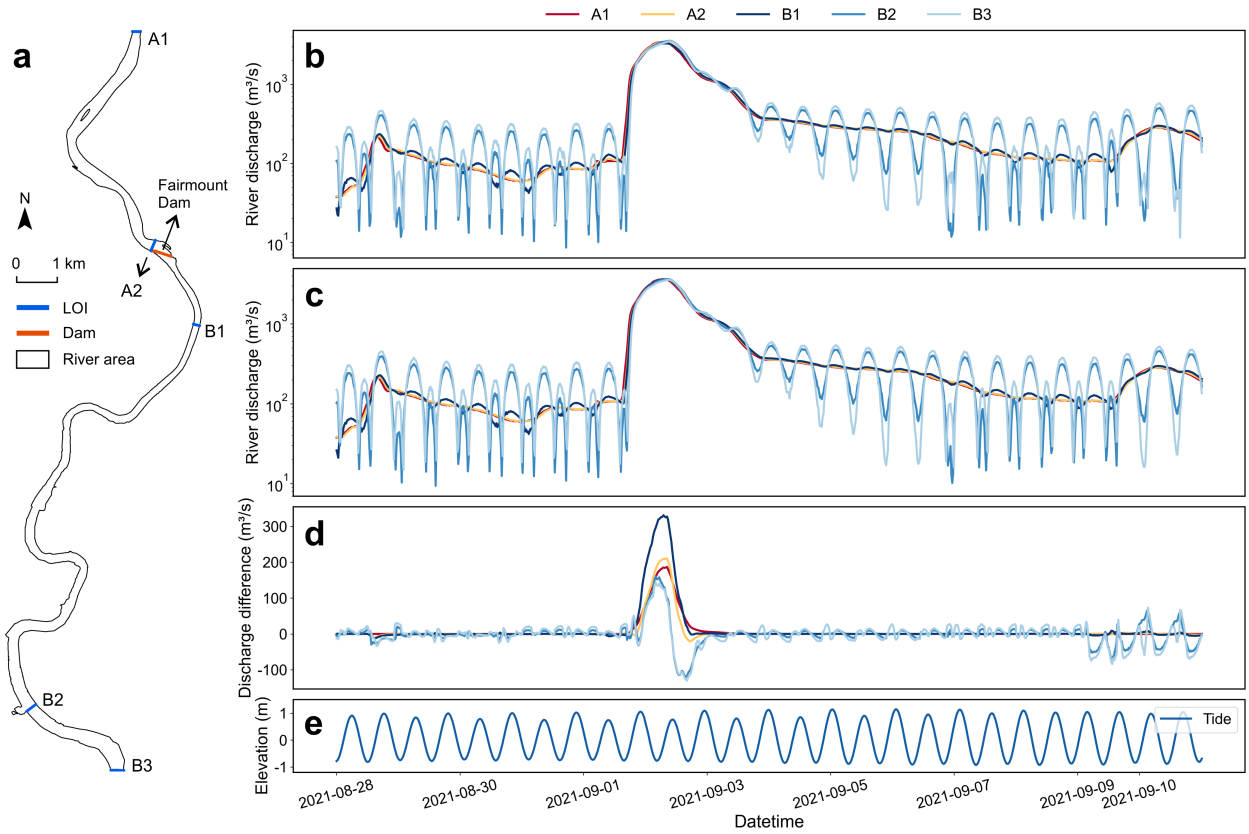


Fig. S5: Correlation between river discharge and tides. (a) Five lines of interests (LOIs), which were chosen at the modeling boundary or close to observation stations. (b, c) Output river discharge above and below the dam in the DTM (b) and the DSM (c). (d) The difference in river discharge between DSM and DTM (i.e., DSM - DTM). (e) Tidal elevation at the outlet (B3).

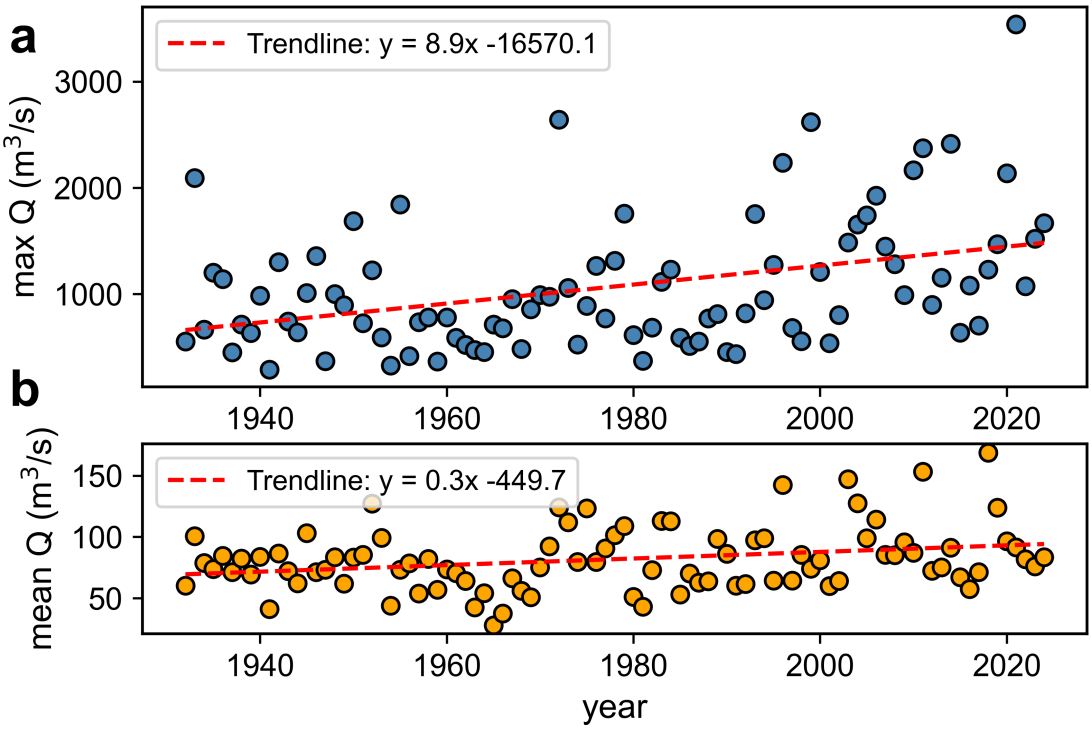


Fig. S6: Time series analysis of annual maximum and average discharge (1932–2024). The red dash lines indicate the fitted trends. The slope coefficients of both trends are statistically significant (p<0.01) based on Monte Carlo tests, demonstrating a clear upward trend over the period. (a) Annual maximum river discharge. (b) Annual average river discharge.

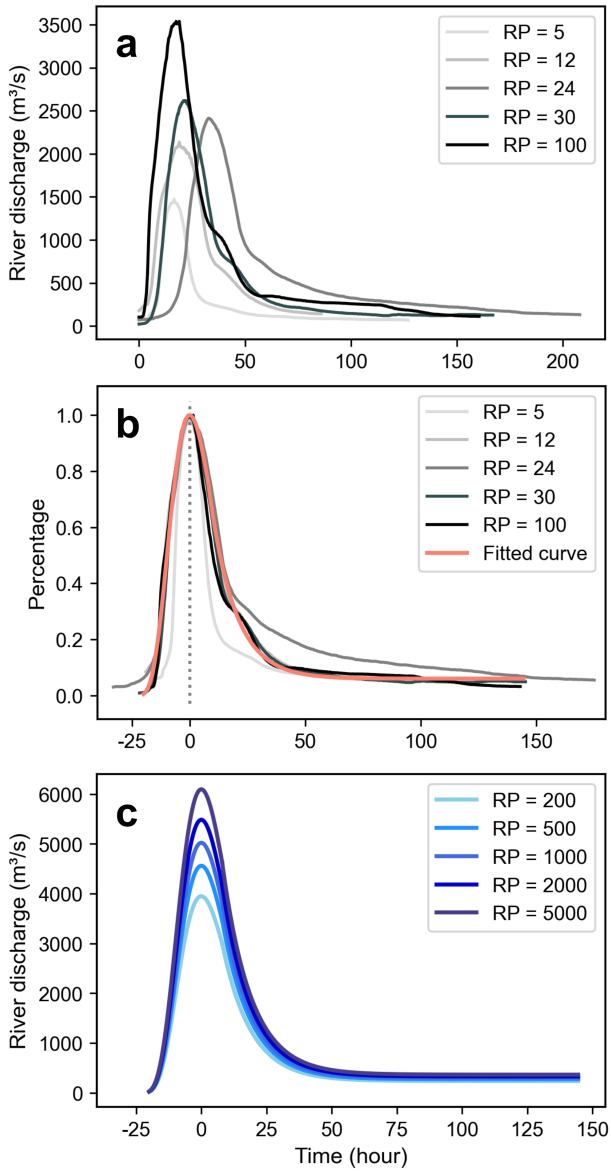


Fig. S7: Observed and designed hydrographs at different return periods (RPs). (a) Single-peak hydrographs chosen from historical periods, with RPs of 5, 12, 24, 30, 100 years corresponding to data from 2003, 2020, 2014, 1999, and 2021, respectively. (b) Standardized hydrographs. Peak time is set to 0 and peak value to 1.0, with each flow value represented as a percentage of the peak. A fitted curve here is estimated to be a generalized framework for designing hydrographs. (c) Design-flood hydrographs for higher RPs based on the fitted curve in panel b, with peak flows calculated using the extrapolation equation from Fig.4a in the main text.

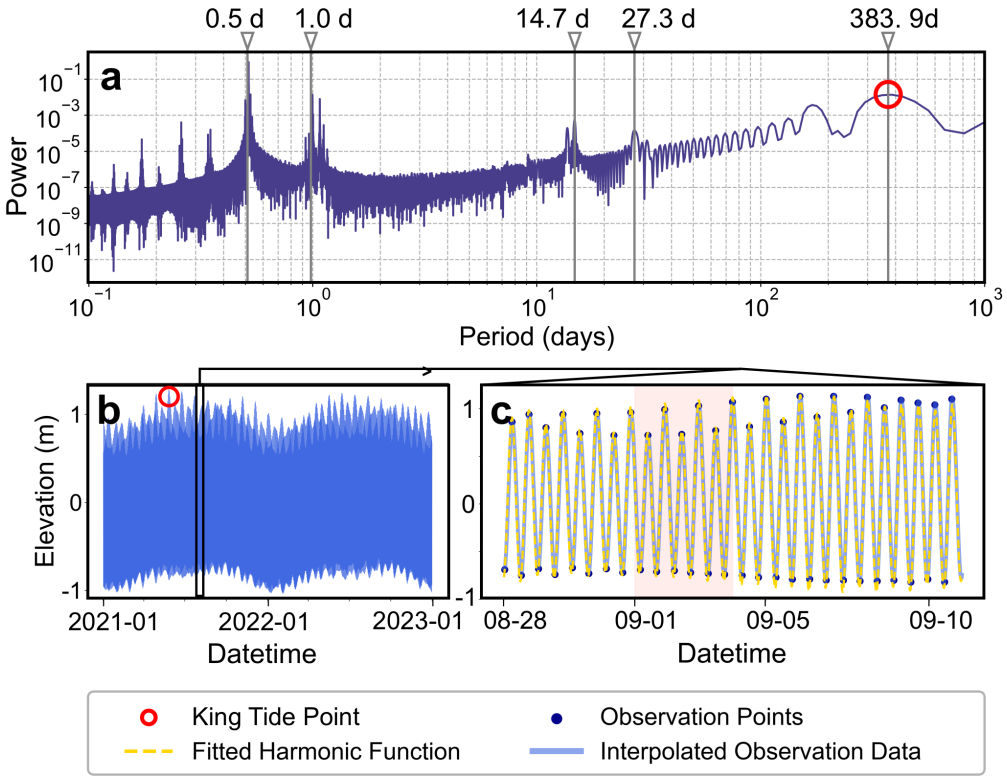


Fig. S8: Tidal periods and elevations. (a) Power spectral density analysis using Lomb-Scargle Periodogram: Triangle markers indicate major tidal periods of the Schuylkill River. (b) Observed tidal elevation for two years collected from NOAA tidal stations, reflecting that the King tide here usually happens once a year. The interpolation method "Spline" was used to get a smooth line of the observation. The black rectangle points the tidal elevation during the 2021 flood event. (c) Comparison of tidal observations and harmonic analysis data during the 2021 flood event. NOAA tidal stations in our research areas provided data on the highest and lowest tides, represented by discrete observation points. We applied a "Spline" method to generate a continuous tidal series, and then used the harmonic analysis to fit the data with a root mean square error (RMSE) of 0.084 m. The light orange shaded area marks the occurrence of the extreme event, which took place between September 1 and September 3, 2021.

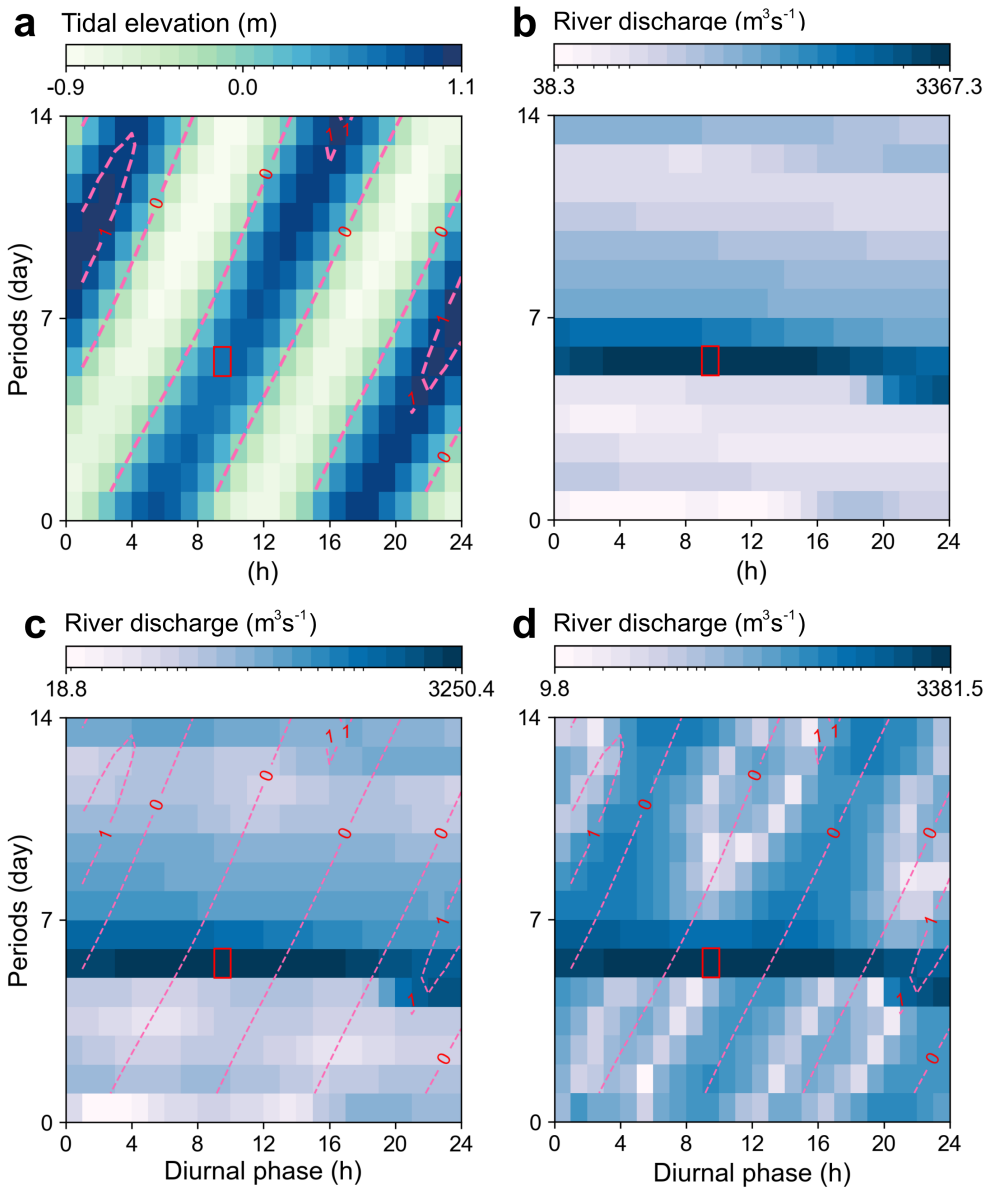


Fig. S9: The impact of tides on river discharges based on the urban catchment. (a) Tidal elevation during the modelling period in terms of diurnal phase and fortnightly periods (Lunar-Solar Phase Plane)[31], with the contour overlaid. The red rectangle indicates the time when river discharge peaked. (b) River discharge above the dam (i.e. at A2 in Fig. **S6**a). (c, d) River discharge below the dam with the same contour in (a): (c) at B1; (d) at B3.

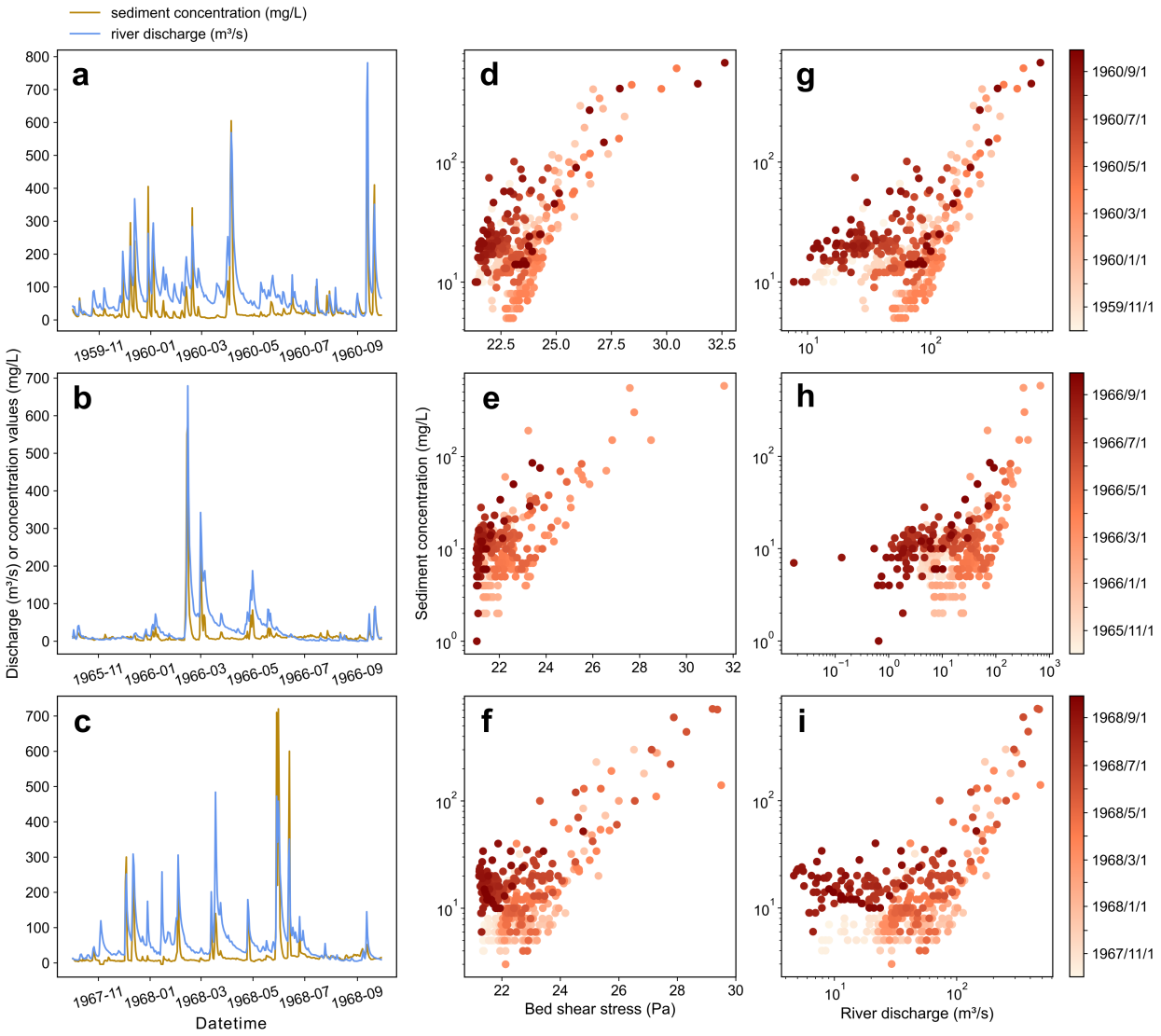


Fig. S10: Relationship between sediment concentration, riverbed shear stress, and river discharge from 1959 to 1968, based on daily average data collected from USGS. The graphs are shown in three separate periods solely due to data gaps. $(a\text{-}c)$ Line charts of sediment concentration and river flows across three different periods. The time periods are chosen due to noncontinuous sediment data availability. $(d\text{-}f)$ Scatter plots that directly show the correlation between bed shear stress and sediment concentration. $(g\text{-}i)$ Scatter plots that directly show the correlation between river discharge and sediment concentration.

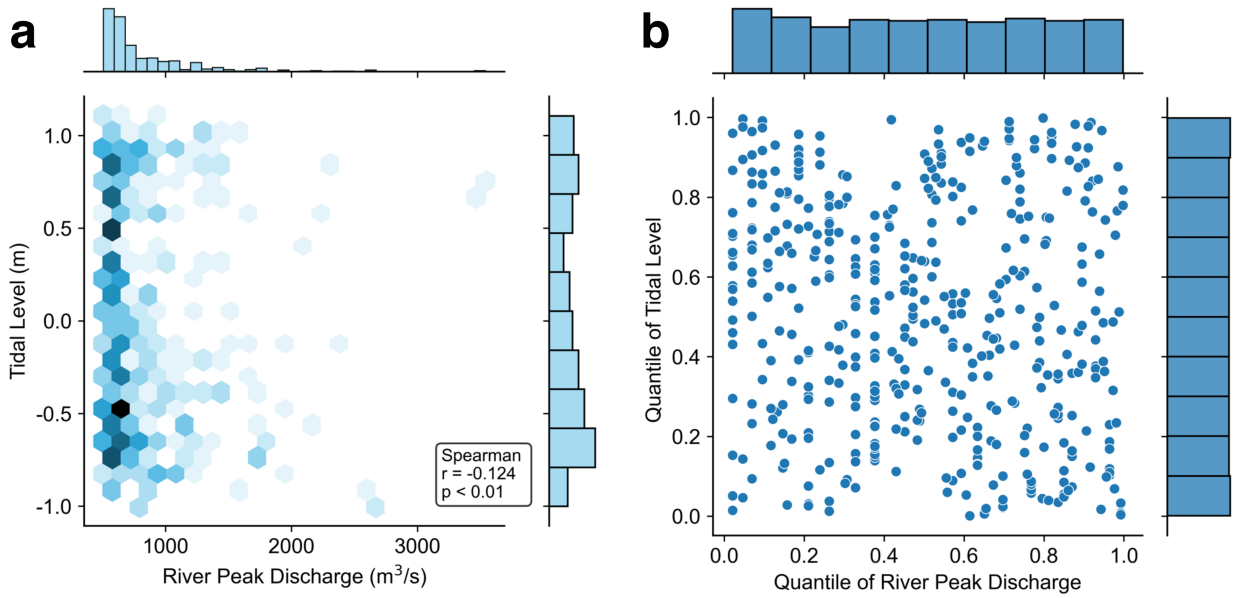


Fig. S11: Dependency between tidal level and river peak discharge in the lower Schuylkill River. (a) The central hexbin plot displays the relationship between river peak discharge and tidal level, with darker color indicating higher data points density. Marginal histograms are shown along the top and right axes, representing the distributions of river peak discharge and tidal level individually. (b) A hexbin plot and marginal histograms of the standardized tidal level and river peak discharge. Higher quantiles correspond to more extreme values (e.g., King tide), while lower quantiles reflect typical or baseline conditions.

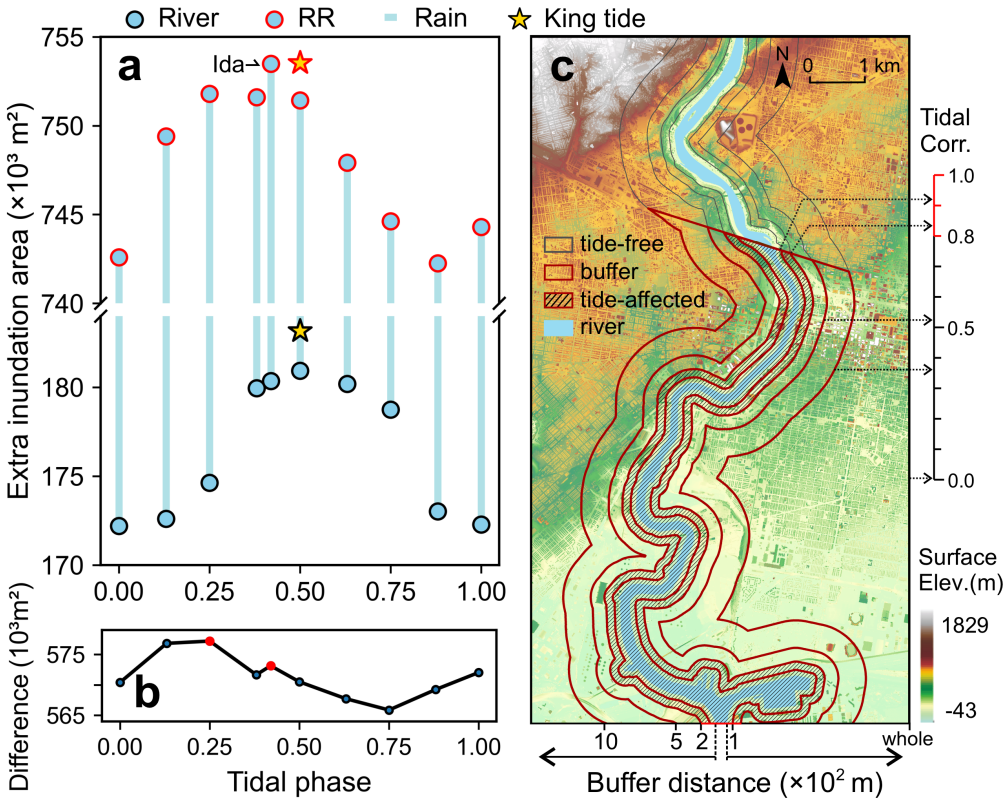


Fig. S12: Maximum inundation areas under varying tidal phases and tidally affected regions along the Schuylkill. (a) Inundation areas for 100-year-RP river flood and compound Rain-Riverine (RR) flood. A 100-meter buffer zone along the riverbank was used to calculate the inundation area during RR events. The difference between River and RR flooding indicates the over-bank inundation induced by accumulative rainfall (b). (c) Buffer zones with and without tidal influences for a compound flood event. All buffers were extended along both riverbanks, focusing on regions below the Fairmount dam, where tidal impacts are considered. The tidal impact was determined by analyzing the correlation between the inundation pattern during this compound flood under varying tidal phases and a semi-diurnal signal from the Schuylkill River, using Spearman's rank correlation coefficient. The tidal correlation values for buffer zones at distances of 100 m, 200 m, 500 m, 1000 m , and across the whole study area are 0.92, 0.83, 0.53, 0.37, 0.03, respectively. Areas with a tidal correlation exceeding 0.8 are considered tidal-affected, with values over 0.9 indicating strong tidal influence. The base map here is a DSM derived from processed LiDAR point cloud data.

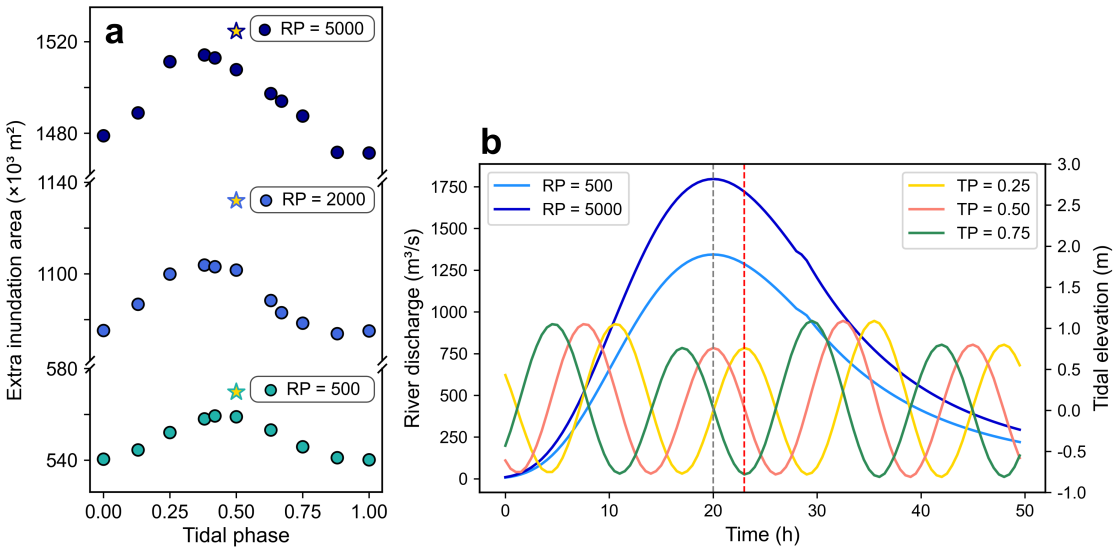
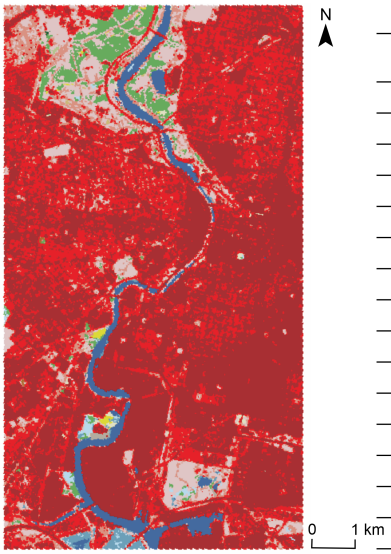


Fig. S13: Maximun inundation patterns for larger river inflows under varying tidal phases (TPs). (a) Maximum river flood inundation areas with river inflows at 500-year, 2000-year, and 5000-year return periods (RPs). The yellow stars represent the inundation area facing the King tide. The corresponding RPs are next to the stars. (b) A visual definition of the relationship between different TPs and river peaks. $TP = 0.5$ is when the tide peak in a semi-diurnal cycle aligns with the river peak. The gray dash line indicates the time when river peaks, while the red one is the time for maximum inundation.



NLCD Topology Value	Description	Manning's Friction (n) Average
11	Open Water	0.038
21	Developed, Open Space	0.040
22	Developed, Low intensity	0.090
23	Developed, Medium Intensity	0.120
24	Developed, High Intensity	0.160
31	Barren Land	0.027
41	Deciduous Forest	0.150
42	Evergreen Forest	0.120
43	Mixed Forest	0.140
52	Shrub/ Scrub	0.115
71/ 72	Herbaceous	0.038
81	Hay/ Pasture	0.038
82	Cultivated Crops	0.035
90	Woody Welands	0.098
95	Emergent Herbaceous Wetlands	0.068

Fig. S14: Land use and land cover of the study area and the Manning's friction reference by National Land Cover Dataset[32].

Supplementary Tables

Table S1: MSM of the river discharge and surface elevation based on DTM and DSM. Locations A1, A2, and B1 are specified in Fig. **S6**

	River discharge		**Surface elevation**	
	A1	A2	A2	B1
DTM	0.997	0.997	0.921	0.940
DSM	0.997	0.998	0.928	0.948

Table S2: Detailed FEMA disaster numbers and associated declared state related to Ida.

FEMA disaster number	State	Declared Date	Declaration Title
EM-3568-LA	LA	Aug-27-2021	TROPICAL STORM IDA
EM-3569-MS	MS	Aug-28-2021	HURRICANE IDA
EM-3572-NY	NY	Sept-02-2021	REMNANTS OF HURRICANE IDA
EM-3573-NJ	NJ	Sept-02-2021	REMNANTS OF HURRICANE IDA
DR-4609-TN	TN	Aug-23-2021	SEVERE STORM AND FLOODING
DR-4611-LA	LA	Aug-29-2021	HURRICANE IDA
DR-4614-NJ	NJ	Sept-05-2021	REMNANTS OF HURRICANE IDA
DR-4615-NY	NY	Sept-05-2021	REMNANTS OF HURRICANE IDA
DR-4618-PA	PA	Sept-10-2021	REMNANTS OF HURRICANE IDA
DR-4626-MS	MS	Oct-22-2021	HURRICANE IDA
DR-4627-DE	DE	Oct-24-2021	REMNANTS OF HURRICANE IDA
DR-4629-CT	CT	Oct-30-2021	REMNANTS OF HURRICANE IDA

Table S3: Verified losses within Philadelphia, within Pennsylvania, and within all affected states.

	(1)	(2)	(3)	(4)	(5)	(6)	(7)	(8)	(9)
	Panel (A): Total Verified Loss (USD)			**Panel (B): Verified Loss Real Estate (USD)**			**Panel (C): Verified Loss Content (USD)**		
	Within Philadelphia	Within Pennsylvania	Within All Affected States	Within Philadelphia	Within Pennsylvania	Within All Affected States	Within Philadelphia	Within Pennsylvania	Within All Affected States
Hurricane Ida × Philadelphia		160,061**	2.137e+06		89,614+	-216,871		70,448***	2.354e+06
		(60,343)	(2.407e+06)		(46,535)	(148,566)		(17,993)	(2.357e+06)
Hurricane Ida	327,207***	177,310***	-1.450e+07	205,556***	127,384***	-1.550e+06*	121,651***	49,926***	-1.295e+07
	(52,132)	(39,009)	(1.269e+07)	(40,072)	(31,137)	(697,551)	(16,195)	(10,503)	(1.241e+07)
Philadelphia		103,924*	-3.354e+06		81,607+	-331,315+		22,318**	-3.023e+06
		(50,443)	(3.001e+06)		(44,484)	(194,099)		(7,166)	(2.923e+06)
Year FE	Yes	Yes	Yes	Yes	Yes	Yes	Yes	Yes	Yes
Zipcode FE	Yes	Yes	Yes	Yes	Yes	Yes	Yes	Yes	Yes
Controls	Yes	Yes	Yes	Yes	Yes	Yes	Yes	Yes	Yes
Observations	901	2,912	16,276	901	2,912	16,276	901	2,912	16,276
R-squared	0.219	0.220	0.094	0.191	0.203	0.159	0.205	0.194	0.088

Note: Panel (A) Total USD amount of losses verified by SBA; Panel (B) USD amount of Real Estate losses verified by SBA; Panel (C) USD amount of the damaged property content (personal property, auto, etc.) verified by SBA. In the models, each observation is zipcode-year SBA request. Some zipcodes have more than one request for a given year. Standard errors clustered at the zipcode level in parentheses. Standard errors clustered at the zipcode level.
*** p<0.001, ** p<0.01, * p<0.05, + p<0.1

Table S4: Approved loan within Philadelphia, within Pennsylvania, and within all affected states.

	(1)	(2)	(3)	(4)	(5)	(6)	(7)	(8)	(9)
	Panel (A): Total Approved Loan Amount (USD)			**Panel (B): Approved Amount Real Estate (USD)**			**Panel (C): Approved Amount Content (USD)**		
	Within Philadelphia	Within Pennsylvania	Within All Affected States	Within Philadelphia	Within Pennsylvania	Within All Affected States	Within Philadelphia	Within Pennsylvania	Within All Affected States
Hurricane Ida × Philadelphia		13,997	-126,226		4,067	-96,049		2,814	-26,787
		(29,572)	(112,336)		(16,954)	(82,045)		(10,143)	(30,315)
Hurricane Ida	108,584***	88,683***	-1.237e+06*	63,703***	56,904***	-957,172*	37,596***	31,858***	-286,483+
	(24,651)	(16,896)	(531,898)	(13,992)	(10,290)	(387,855)	(6,727)	(8,110)	(148,333)
Philadelphia		55,832+	-267,782+		33,655*	-214,348*		9,098**	-67,883+
		(31,250)	(145,802)		(15,947)	(103,663)		(3,169)	(37,206)
Year FE	Yes	Yes	Yes	Yes	Yes	Yes	Yes	Yes	Yes
Zipcode FE	Yes	Yes	Yes	Yes	Yes	Yes	Yes	Yes	Yes
Controls	Yes	Yes	Yes	Yes	Yes	Yes	Yes	Yes	Yes
Observations	901	2,912	16,276	901	2,912	16,276	901	2,912	16,276
R-squared	0.166	0.177	0.133	0.162	0.169	0.132	0.181	0.161	0.123

Note: Panel (A) Total USD amount of approved SBA disaster home loan; Panel (B) USD amount of approved Real Estate loan proceeds; Panel (C) USD amount of approved content loan proceeds. In the models, each observation is zipcode-year SBA request. Some zipcodes have more than one request for a given year. Standard errors clustered at the zipcode level in parentheses. Standard errors clustered at the zipcode level.
*** p<0.001, ** p<0.01, * p<0.05, + p<0.1

Table S5: Average and total net present values (NPV) with varied discount rates and three default rates.

Panel (A): Average NPV

Default Rate (%) \ Discount Rate (%)	1%	3%	5%	7%	9%	11%
0%	$ (158,088.78)	$ (162,165.19)	$ (164,908.25)	$ (166,810.14)	$ (168,167.47)	$ (169,163.13)
10%	$ (159,685.70)	$ (163,354.47)	$ (165,823.22)	$ (167,534.92)	$ (168,756.53)	$ (169,652.61)
20%	$ (161,282.63)	$ (164,543.75)	$ (166,738.20)	$ (168,259.70)	$ (169,345.58)	$ (170,142.09)

Panel (B): Total NPV

Default Rate (%) \ Discount Rate (%)	1%	3%	5%	7%	9%	11%
0%	$ (19,919,186.44)	$ (20,432,813.63)	$ (20,778,439.50)	$ (21,018,077.72)	$ (21,189,101.06)	$ (21,314,553.75)
10%	$ (20,120,398.59)	$ (20,582,663.06)	$ (20,893,725.56)	$ (21,109,400.16)	$ (21,263,322.94)	$ (21,376,228.78)
20%	$ (20,321,610.75)	$ (20,732,512.50)	$ (21,009,013.59)	$ (21,200,722.59)	$ (21,337,542.84)	$ (21,437,903.81)

Table S6: Detailed bridge names

Bridge abbreviation	Full names
Vine St. Br.	Vine Street Bridge
Market St. Br.	Market Street Bridge
Walnut St. Br.	Walnut street Bridge
South St. Br.	South Street Bridge
Univ. Ave. Br.	University Avenue Bridge
B&O RR. Br.	B&O Railroad Bridge
Passyunk Ave. Br.	Passyunk Avenue Bridge

Table S7: Detailed parameters of Fourier modes

Tidal components	A_{i} (m)	T_{i} (day)	ϕ_{i}
1. M_2 ($\mathrm{i}=1$)	0.892	0.518 (12.422 h)	-1.050
2. S_2 ($\mathrm{i}=2$)	-0.086	0.500 (12.004 h)	-0.279
3. K_1 ($\mathrm{i}=3$)	-0.089	0.996 (23.915 h)	-0.277
4. O_1 ($\mathrm{i}=4$)	-0.065	1.079 (25.886 h)	0.890

References

[1] Paul D Bates and APJ De Roo. A simple raster-based model for flood inundation simulation. *Journal of hydrology*, 236(1-2):54–77, 2000.

[2] Mark A Trigg, Matthew D Wilson, Paul D Bates, Matthew S Horritt, Douglas E Alsdorf, Bruce R Forsberg, and Maria C Vega. Amazon flood wave hydraulics. *Journal of Hydrology*, 374(1-2):92–105, 2009.

[3] Jeffrey Neal, Guy Schumann, and Paul Bates. A subgrid channel model for simulating river hydraulics and floodplain inundation over large and data sparse areas. *Water Resources Research*, 48(11), 2012.

[4] Paul D Bates, Matthew S Horritt, and Timothy J Fewtrell. A simple inertial formulation of the shallow water equations for efficient two-dimensional flood inundation modelling. *Journal of hydrology*, 387(1-2):33–45, 2010.

[5] James Shaw, Georges Kesserwani, Jeffrey Neal, Paul Bates, and Mohammad Kazem Sharifian. Lisflood-fp 8.0: the new discontinuous galerkin shallow-water solver for multi-core cpus and gpus. *Geoscientific Model Development*, 14(6):3577–3602, 2021.

[6] Mohammad Kazem Sharifian, Georges Kesserwani, Alovya Ahmed Chowdhury, Jeffrey Neal, and Paul Bates. Lisflood-fp 8.1: new gpu-accelerated solvers for faster fluvial/pluvial flood simulations. *Geoscientific Model Development*, 16(9):2391–2413, 2023.

[7] Alice K Li, Yue Mao, Sandeep Manjanna, Sixuan Liu, Jasleen Dhanoa, Bharg Mehta, Victoria M Edwards, Fernando Cladera Ojeda, M Ani Hsieh, Maël Le Men, et al. Towards understanding underwater weather events in rivers using autonomous surface vehicles. In *OCEANS 2022, Hampton Roads*, pages 1–8. IEEE, 2022.

[8] Youtong Rong, Paul Bates, and Jeffrey Neal. Gpu-accelerated urban flood modeling using a nonuniform structured grid and a super grid scale river channel. *Water Resources Research*, 60(6):e2023WR036128, 2024.

[9] Leanne Archer, Jeffrey Neal, Paul Bates, Emily Vosper, Dereka Carroll, Jeison Sosa, and Daniel Mitchell. Current and future rainfall-driven flood risk from hurricanes in puerto rico under 1.5 and 2 c climate change. *Natural Hazards and Earth System Sciences*, 24(2):375–396, 2024.

[10] L Mullen and PR Herczfeld. Application of radar technology to aerial lidar systems. In *1994 IEEE MTT-S International Microwave Symposium Digest (Cat. No. 94CH3389-4)*, pages 175–178. IEEE, 1994.

[11] Chia-Yu Wu, Joann Mossa, Liang Mao, and Mohammad Almulla. Comparison of different spatial interpolation methods for historical hydrographic data of the lowermost mississippi river. *Annals of GIS*, 25(2):133–151, 2019.

[12] Venkatesh Merwade. Effect of spatial trends on interpolation of river bathymetry. *Journal of Hydrology*, 371(1-4):169–181, 2009.

[13] Oliver EJ Wing, Paul D Bates, Christopher C Sampson, Andrew M Smith, Kris A Johnson, and Tyler A Erickson. Validation of a 30 m resolution flood hazard model of the conterminous u nited s tates. *Water Resources Research*, 53(9):7968–7986, 2017.

[14] U.S. Small Business Administration. Disaster loan data. `https://data.sba.gov/en/dataset/disaster-loan-data`. Last Updated: May-8-2024.

[15] Federal Emergency Management Agency. Disaster declarations summaries - v2. `https://www.fema.gov/openfema-data-page/disaster-declarations-summaries-v2`, 2025. Last Data Refresh: Oct-26-2025.

[16] Anna Josephson and Maria I Marshall. The demand for post-Katrina disaster aid: SBA disaster loans and small businesses in Mississippi. *Journal of Contingencies and Crisis Management*, 24(4):264–274, 2016.

[17] Benjamin L Collier, Sabrina T Howell, and Lea Rendell. After the storm: How emergency liquidity helps small businesses following natural disasters. Technical report, National Bureau of Economic Research, 2024.

[18] Joshua D Angrist and Jörn-Steffen Pischke. *Mostly harmless econometrics: An empiricist's companion*. Princeton university press, 2009.

[19] Scott Cunningham. *Causal inference: The mixtape*. Yale university press, 2021.

[20] A Colin Cameron and Douglas L Miller. A practitioner's guide to cluster-robust inference. *Journal of human resources*, 50(2):317–372, 2015.

[21] Aswath Damodaran. *Investment valuation: Tools and techniques for determining the value of any asset*. John Wiley & Sons, 2012.

[22] U.S. Small Business Administration (SBA). Sba tops $1 billion in disaster assistance loans for hurricane ida, November 2021. Accessed on October 25, 2025.

[23] Monomoy Goswami. Generating design flood hydrographs by parameterizing the characteristic flood hydrograph at a site using only flow data. *Hydrological Sciences Journal*, 67(16):2505–2523, 2022.

[24] Jacob T VanderPlas. Understanding the lomb–scargle periodogram. *The Astrophysical Journal Supplement Series*, 236(1):16, 2018.

[25] Colin B Phillips, Claire C Masteller, Louise J Slater, Kieran BJ Dunne, Simona Francalanci, Stefano Lanzoni, Dorothy J Merritts, Eric Lajeunesse, and Douglas J Jerolmack. Threshold constraints on the size, shape and stability of alluvial rivers. *Nature Reviews Earth & Environment*, 3(6):406–419, 2022.

[26] Renato Prata de Moraes Frasson, Tamlin M Pavelsky, Mark A Fonstad, Michael T Durand, George H Allen, Guy Schumann, Christine Lion, R Edward Beighley, and Xiao Yang. Global relationships between river width, slope, catchment area, meander wavelength, sinuosity, and discharge. *Geophysical Research Letters*, 46(6):3252–3262, 2019.

[27] Konstantinos M Andreadis, Guy J-P Schumann, and Tamlin Pavelsky. A simple global river bankfull width and depth database. *Water Resources Research*, 49(10):7164–7168, 2013.

[28] Khawla Ali Abd Al-Hameed. Spearman's correlation coefficient in statistical analysis. *International Journal of Nonlinear Analysis and Applications*, 13(1):3249–3255, 2022.

[29] Statistical Atlas, United States Census Bureau. Map of population by tract in philadelphia county. `https://statisticalatlas.com/county/Pennsylvania/Philadelphia-County/Population`, 2018. Accessed: 2023-May-01.

[30] Sebastian J Interlandi and Christopher S Crockett. Recent water quality trends in the schuylkill river, pennsylvania, usa: a preliminary assessment of the relative influences of climate, river discharge and suburban development. *Water research*, 37(8):1737–1748, 2003.

[31] Hugo N Ulloa, Kristen A Davis, Stephen G Monismith, and Geno Pawlak. Temporal variability in thermally driven cross-shore exchange: The role of semidiurnal tides. *Journal of Physical Oceanography*, 48(7):1513–1531, 2018.

[32] USGS. National land cover database. `https://www.usgs.gov/centers/eros/science/national-land-cover-database`, 2021. Accessed: 2023-May-01.